NUCLEAR STRUCTURE -- THEORY

PROTON HALOS IN THE $1s0d$ SHELL

B. A. Brown and P. G. Hansen

Nuclei near the proton and neutron drip lines often have matter distributions which extend to large radii due to the loose binding of the last one or two nucleons. The extended distributions are referred to as "halos". [1,2] The halo has been observed experimentally from an increase of the total reaction cross section, which is related to the total matter density, and from the momentum distribution in break-up reactions, which is related to the density of the valence orbital. One of the simplest ground-state examples is ^{11}Be where the last neutron is predominantly in a $1s_{1/2}$ state [3] and is bound only by 0.50 MeV. The density distribution of the valence neutron is extended with an rms radius [2,4,5] of about 6.0 fm, and the parallel-momentum distribution in the reaction (^{11}Be,^{10}Be) is correspondingly narrow, [6] 42±2 MeV/c for a light target, due of the loose binding, and because there is no centrifugal or Coulomb barrier. There is a similar case which has been recently studied [7,8] in ^{19}C. Other examples [1,2,5] on the neutron-rich side are the loosely bound di-neutron systems such as ^{11}Li and ^{14}Be.

The analogues of the cases mentioned above on the proton-rich side are all unbound. Perhaps the simplest example of a bound-state proton halo is that of the $1/2^+$ first excited state of ^{17}F which is bound by 0.10 MeV. This state is described in zeroth order by a $1s_{1/2}$ configuration outside of an ^{16}O closed shell, and has a calculated [9] rms valence radius of 5.5 fm. However, since this is an excited state its reaction cross section and momentum distribution cannot be studied, and its proton halo nature is inferred from the large Thomas-Ehrman Coulomb shift relative to the $5/2^+$ T=1/2 ($0d_{5/2}$) ground state [10,11] and from the large $1/2^+$ to $5/2^+$ B(E2) value. [9] In general, for a fixed angular momentum and fixed separation energy, the size of the proton halo states are not as large as the neutron halo states because of the Coulomb barrier.

The only case on the proton-rich side whose break-up distribution of parallel momentum has been studied is that of ^{8}B. (We restrict the discussion of momentum distributions to the parallel momentum measured in reactions such as (^{26}P,^{25}Si) etc. on light targets because this parameter seems particularly simple to interpret. It should be clear that valuable additional characterization of halo states can be obtained from the transverse momentum components and from Coulomb excitation of the halo.) The valence proton in this case is bound by 0.137 MeV and the calculated [12] valence $0p$ proton rms radius is 4.4 fm. Its measured momentum distribution [13,14] is, however, almost a factor of two narrower than that predicted from the Fourier transform of the spatial wave function of the valence nucleon, and this is presumably [12,15] related to the fact that the proton stripping reaction only samples the valence density beyond a minimum impact parameter b_{min}. This can be defined as the sum of the (experimentally determined) energy-dependent interaction radii of the core fragment and the target. For ^{8}B incident at 1.47 GeV/u on a carbon target one has a b_{min} of 4.8 fm. An estimate based on an eikonal picture can account both for the momentum content of the halo wave function and for the absolute cross section, which can be linked to that for free nucleons of the same velocity. The effects of the localization of the reaction to the external part of the wave function are strongly dependent on the separation energy of the halo nucleon and its angular momentum. In the case of a neutron in an s state with parameters corresponding to those of ^{11}Be, the momentum width is rather close to that of the wave function as a whole, which is probably why the localization effect was not considered in early discussions of the parallel-momentum distributions.

The main thing missing from the cases discussed above is a good example of a proton-rich ground

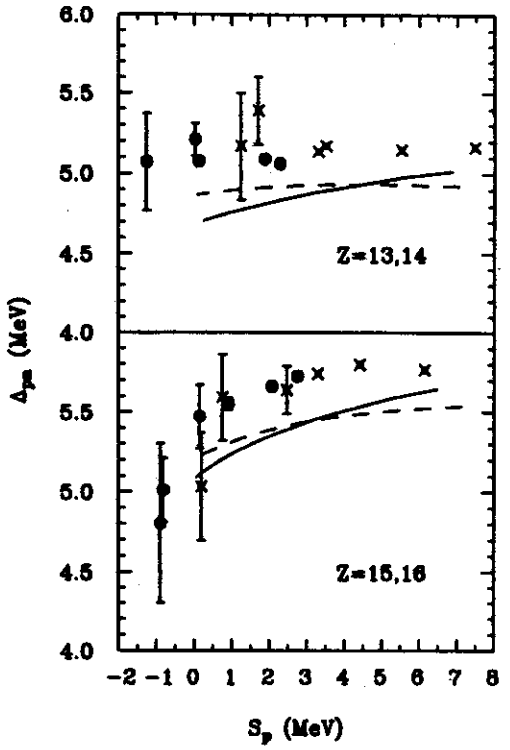

Figure 1: Δ_{pn} vs S_p. The experimental results [18] for Z=13 and Z=15 are given by the filled circles. The experimental results for Z=14 and Z=16 multiplied by (13/14) and (15/16), respectively, are given by crosses. The solid and dashed lines for Z=13,14 are the $0d_{5/2}$ calculations discussed in the text. The solid and dashed lines for Z=15,16 are the $1s_{1/2}$ calculations discussed in the text.

state whose structure is that of a valence proton $s_{1/2}$ orbital coupled to the ground state of the core. The natural place to look for such a configuration is in the middle of the $1s0d$ shell at the nuclei with Z=15 and Z=16, where in the simplest shell-model picture the $1s_{1/2}$ orbital becomes filled. An example is ^{29}P which is well known [16] to have a zeroth-order structure of a $1s_{1/2}$ proton outside a ^{28}Si closed shell, but its structure is not as simple as that of ^{17}F, and the full-$1s0d$ shell configuration mixing is needed [16,17] in order to explain the magnetic properties of ^{29}P and its mirror ^{29}Si. It is interesting to examine the properties of the more proton-rich isotopes of phosphorus (Z=15).

The one-proton separation energies, S_p, for the Z=15 isotopes as a function of neutron number N can be obtained from Ref [18]. It clear that ^{26}P is potentially the most interesting loosely bound case, as has been pointed out recently on the basis of relativistic mean-field calculations, [19] and it is known [20] to be particle-stable.

The quantitity S_p, for the Z=15 isotopes can be compared with the one-neutron separation energies [18], S_n, for N=15 as a function of proton number. The quantity $\Delta_{pn} = S_p - S_n$ is the generalized Coulomb shift. It can be modeled by calculating the proton and neutron single-particle energies in a Woods-Saxon potential which has a Coulomb potential plus a common central potential for protons and neutrons. By varying the depth and/or radius of the central potential one can calculate the relationship between S_p and Δ_{pn}. The results for a typical Woods-Saxon potential are shown in Fig. 1 and compared to experiment. The solid line is the result obtained by varying the well depth for a fixed radius ($R = 3.89$ fm) and diffuseness ($a = 0.65$ fm), and the dashed line is the result obtained by varying the radius for a fixed well depth and diffuseness. The main point is that the calculated dependence of Δ_{pn} upon S_p

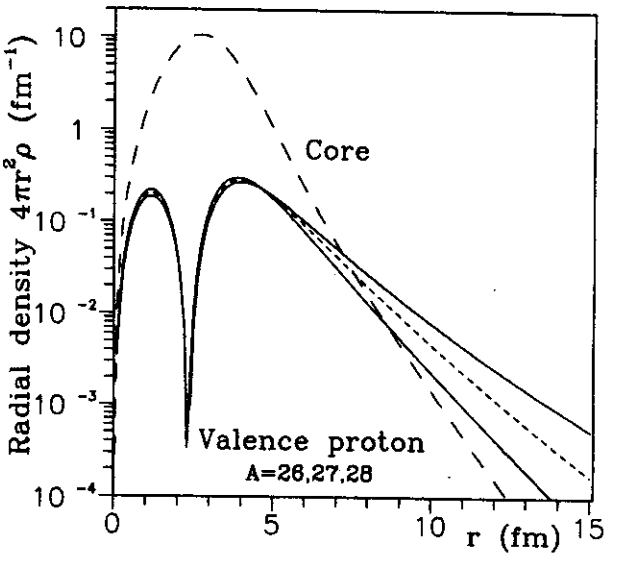

Figure 2: The radial density probability distribution of the core and of the valence proton, the latter calculated in a single particle Woods-Saxon model for ^{26,27,28}P with proton separation energies assumed to be 0.14, 0.90 and 2.07 MeV, respectively. The valence proton distribution is normalized to unity.

is very smooth even very close to the proton threshold (when S_p goes to zero). This is because of the relatively large Coulomb barrier. The experimental values show a similar behavior. Taking into account this smooth behaviour, the S_p value for ^{26}P should be close to the Audi-Wapstra extrapolation of 0.14 MeV, and its uncertainty must be nearly an order of magnitude smaller than their estimated value of 0.20 MeV. (The overall shift between the experimental and theoretical values is related to the Nolen-Schiffer anomaly and as well as the various exchange-interaction and relativistic corrections which are left out of the calculation. [10])

The slope for the $1s_{1/2}$ state seen in Fig. 1 is related to the Thomas-Ehrman shift for the $1s_{1/2}$ halo state. It is interesting to compare these results for the $1s_{1/2}$ configuration to those for the isotopes with Z=13 and Z=14 which should be dominated by a $0d_{5/2}$ valence configuration, see Fig. 1. In this case the experimental values for Δ_{pn} are essentially flat as a function of S_p, and this is reproduced by the calculation for the $0d_{5/2}$ in which the radius is varied (the dashed line). The calculated curve for $0d_{5/2}$ shows a smaller slope relative to $0s_{1/2}$ due to the centrifugal barrier for ℓ=2.

The case of ^{26}P is more complicated than the usual one-nucleon halos because it has an odd number of both neutrons and protons. The properties of the mirror nucleus, ^{26}Na, have been obtained from β decay experiments [21,22] In particular it has a ground state spin of 3^+ and this is thus the most likely spin for the ground state of the mirror nucleus ^{26}P. In the full $0d1s$ shell-model calculation [23,24] its main parentage is to the $5/2^+$ ground state of ^{25}Si with a $1s_{1/2}$ spectroscopic factor of $C^2S = 0.66$ (to be compared with $C^2S = 1.0$ in the zeroth-order shell model). The $0d_{5/2}$ spectroscopic factor is very small (0.002). The total proton occupation of the $1s_{1/2}$ orbital is 1.05 and the remaining 0.39 of the $1s_{1/2}$ spectroscopic strength goes to highly excited $5/2^+$ and $7/2^+$ states in ^{25}Si.

The halo structure of ^{26}P should thus be calculated as if it were 0.66 of $1s_{1/2}$ proton bound by about 0.14 MeV to the ^{25}Si ground state. In a typical Woods-Saxon geometry (the same one used in the discussion above), the rms radius of the $1s_{1/2}$ state is 4.71 fm. This can be compared to the total proton and neutron rms radius of the ^{25}Si core of 3.35 fm and 2.86 fm, respectively, see Fig. 2.

The behavior of the single-particle proton wave functions at large distances is dominated by the

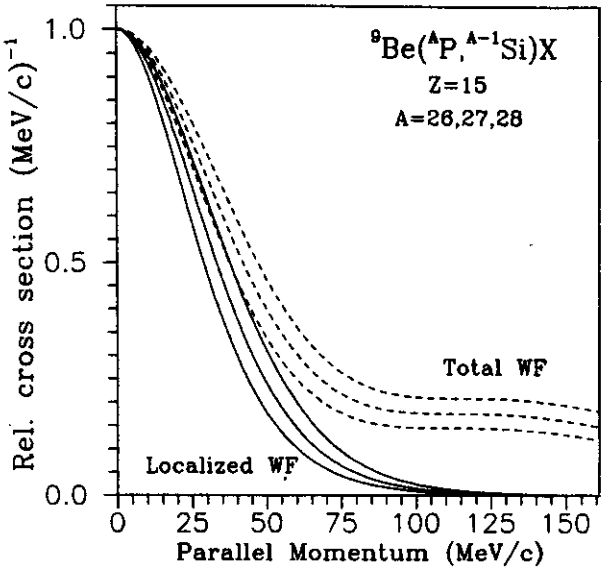

Figure 3: The parallel-momentum distributions calculated for the ^{26,27,28}P proton halos with parameters as in Fig. 2. The curves for mass 26 are those most to the left. The dashed curves represent the result for the total wave function. The full-drawn curves take into account that the interaction with the target (taken to be ^{9}Be) localizes the observation to distances beyond the minimum impact parameter. Note that in the latter case the complete disappearance of the plateau around 100-150 MeV/c representing the inner lobe of the spatial wave functions (Fig. 2).

Coulomb barrier and the sensitivity to the proton separation energy is not large. This can be seen from the comparison of the radial densities for ^{26,27,28}P shown in Fig. 2, and which correspond to rms radii of 4.71, 4.37 and 4.11 fm, respectively. For comparison a corresponding $1s$ state neutron with an S_n of 0.14 MeV would have a radius of about 10.8 fm.

Not surprisingly, the calculated parallel-momentum distributions shown in Fig. 3 mirror closely the behavior of the spatial wave functions. The approximation used here for calculating the localization effect replaces the wave function in the tube swept by the target nucleus by its values along the axis defined by the impact parameter, the minimum of which is 6.2 fm for the case of a ^{9}Be target. Due to the strong effect of the Coulomb barrier, which makes the external wave function fall off more rapidly, this approximation is less accurate than previous estimates [15] for lighter systems. It should give reasonable values for the momentum distributions but will underestimate the cross sections. For an assumed beam energy of 60 MeV/u and for phosphorus isotopes with masses 26, 27 and 28, the calculated localized widths are 58 (74), 66 (84) and 75 (94) MeV/c, respectively, for the full width at half maximum. The values in parentheses are those calculated for the total wave function. The corresponding calculated cross sections (assuming $C^2S = 1$) are 51, 35 and 22 mb, respectively, very similar to those of single-nucleon knock-out reactions on systems with normal binding.

It is feasible and should be very interesting to study the parallel momentum distributions experimentally. The best illustration [12,15] of the localization effect so far, that of the ^{8}B 0p state, has a single lobe in the wave function and the effect shows up as a narrowing of the observed distribution. In contrast to this, the absence in the phosphorus isotopes of the large momentum components corresponding to the inner lobe of the $1s$ state will provide another experimental signature for the contribution from the reaction mechanism.

It is also interesting to investigate the proton-halo aspects of the Z=16 isotopes. It would appear

from the Audi-Wapstra mass systematics that ^{26}S could be a loosely bound system, and this would be particularly interesting since the corresponding daughter nucleus ^{25}P is itself unbound. However, from the Δ_{pn} systematics it is clear that Δ_{pn} should be close to 6.0 MeV which when combined with S_n for ^{26}Na would make ^{26}S unbound by 0.42(7) MeV. In addition, ^{26}S is unbound to two-proton emission. ^{27}S has a separation energy of 0.75 MeV. The properties of the $1s_{1/2}$ halo in ^{27}S should be very similar to that of ^{27}P shown in Figs. 2 and 3, since the one-proton separation energy is about the same in both cases. As pointed out in Ref 19, ^{27}S also has the property of a relatively loosely bound di-proton system. It would be very interesting to try to apply the three-body techniques which have been used for ^{11}Li to the case of ^{27}S.

References

1. A. C. Mueller and B. M. Sherrill, Annu. Rev. Nucl. Part. Sci. 43, 529 (1993).
2. P. G. Hansen, A. S. Jensen and B. Jonson, Annu. Rev. Nucl. Part. Sci. 45, 591 (1995).
3. H. Sagawa, B. A. Brown and H. Esbensen, Phys. Lett. B309, 1 (1993); T. Otsuka, N. Fukunishi and H. Sagawa, Phys. Rev. Lett. 79, 1385 (1993); H. Esbensen, B. A. Brown and H. Sagawa, Phys. Rev. C51, 1274 (1995).
4. D. J. Millener, J. W. Olness, E. K. Warburton and S. S. Hanna, Phys. Rev. C28, 497 (1983).
5. G. F. Bertsch, B. A. Brown and H. Sagawa, Phys. Rev. C39, 1154 (1989).
6. J. H. Kelley et al., Phys. Rev. Lett. 74, 30 (1995).
7. D. Bazin et al., Phys. Rev. Lett. 74, 3569 (1995).
8. F. M. Marques et al., IPC CAEN preprint LPCC 96-05.
9. B. A. Brown, A. Arima and J. B. McGrory, Nucl. Phys. A277, 77 (1977).
10. J. Nolen and J. P. Schiffer, Annu. Rev. Nucl. Sci. 19, 471 (1969).
11. R. Sherr and G. Bertsch, Phys. Rev. C32, 1809 (1985).
12. B. A. Brown, A. Csoto and R. Sherr, Nucl. Phys. A597, 66 (1996).
13. W. Schwab et al., Z. Phys. A350, 283 (1995).
14. J. H. Kelley et al., Bull. Am. Phys. Soc. 40, 978 (1995).
15. P. G. Hansen, Proceedings of the International Conference on Exotic Nuclei and Atomic Masses Conference, Arles 1995, edited by M. de Saint Simon and O. Sorlin, (Editions Frontieres) in press, and to be published.
16. B. A. Brown, Nucl. Phys. A522, 221c (1991).
17. B. A. Brown, R. Radhi and B. H. Wildenthal, Phys. Lett. 133B, 5 (1983).
18. G. Audi and A. H. Wapstra, Nucl. Phys. A595, 409 (1995).
19. Z. Ren, B. Chen, Z. Ma and G. Xu, Phys. Rev. C53, R572 (1996).
20. M. D. Cable et al., Phys. Rev. C30, 1276 (1984).
21. P. M. Endt, Nucl. Phys. A521, 1 (1990).
22. J. P. Dufour, private communication.
23. B. A. Brown and B. H. Wildenthal, Annu. Rev. Nucl. Sci. 38, 29 (1988).
24. B. A. Brown, W. A. Richter, R. E. Julies and B. H. Wildenthal, Ann. Phys. 182, 191 (1988).

THE MOMENTUM CONTENT OF SINGLE-NUCLEON HALOS

P.G. Hansen

It is commonly assumed that the longitudinal momentum distributions of the core fragment in stripping and diffraction dissociation of halo states represent the true momentum distribution of the halo state. This would imply that experiments on a single-nucleon halo measured the square of the Fourier transform of the total wave function. It has recently been suggested [1,2] that the information actually obtained is more specific and, in fact, more interesting. The essential point is that the reactions that remove the halo nucleon sample only a region of space localized outside of the nuclear core. The core-target collisions at small impact parameters lead to other exit channels, mainly complex fragmentation reactions. When this is taken into account, the calculations agree well with the recently measured [3-5] momentum widths and cross sections for the reactions (^{11}Be, ^{10}Be) and (^{8}B, ^{7}Be) on light targets. The essential points of the argument are given in the following. A by-product of some importance for the analysis of experiments is that the measured widths are expected to be independent of the instrumental transverse-momentum acceptance.

The analysis of reactions with light targets is simplified by a number of favorable circumstances. The spatially extended halo states are well represented in terms of a wave function ψ_0 based on a single-particle potential-well model. The reactions producing a fast core fragment have contributions from two reaction channels, and because the beam velocity is much higher than that of the halo nucleon, both can be treated in the sudden approximation. In the first, referred to as nucleon stripping (or absorption), the halo nucleon has interacted strongly with the target and disappears from the beam. In the second channel, referred to as diffraction dissociation, the nucleon moves forward with essentially beam velocity.

The high projectile energies, 0.5-12 GeV, imply that the collision may be described in terms of a classical impact parameter, so that the dissociation reactions are characteristic of impact parameters greater than $b_{min}=R_C+R_A$, defined as the sum of the energy-dependent core and target interaction radii known from measured interaction cross sections. The high energy also means that the eikonal approximation is applicable. Hence the target trajectory is a straight line and the range of the interaction (which does not have to be weak) is of the order of the effective target radius R_a, so that the wave function of the halo state remains unchanged throughout all space except in a cylinder of radius R_a, and inside of which it can be set to zero. This is the simplest form of the Glauber model. The effective target radius can be chosen so that the stripping and diffraction cross-sections coincide with the experimental reaction and elastic cross sections for free nucleons in the limit $b_{min}=0$.

In the sudden approximation the nucleon stripping reaction selects at the moment of impact the state of the system to be $\delta\psi_0$, the wave function contained in the tube swept by the target. The normalization P_a of this state is the reaction probability for a given b, and square of its three-dimensional Fourier transform gives the momentum distribution, which must be that of the core fragment since the halo nucleon is no longer present. For the same reason, the question of final-state interactions does not arise. The state represented by the complement of the wave function ψ_0-$\delta\psi_0$ is mainly the unchanged halo state. The (small) probability that it decays by diffraction dissociation is obtained directly if it is assumed that the only bound state of the system is the halo state ψ_0, which can be projected out to give the wave function of the decaying state $\psi_d = P_a\psi_0-\delta\psi_0$ with normalization of $P_a-P_a^2$. It will be seen that the first term in the wave function of the decaying state is a small correction, necessary to preserve orthogonality, and that it contributes intensities of second order only in the small quantity P_a. Hence the probabilities of stripping and diffraction dissociation are approximately identical

and equal to P_a, a result that is related to the fact that fast-neutron total cross sections are approximately twice the geometrical value. If final-state interactions can neglected, the momentum distribution for diffraction dissociation is also given by the square of the Fourier transform of $\delta\psi_0$. The parallel momentum distribution is then obtained by integrating over the two unobserved directions.

Results for the case of the 1*s* neutron of ^{11}Be are shown in Fig.1 as a function of the impact parameter b. As the integrals over the intersection of a cylinder with the wave function are not very convenient, the calculations have been carried out in two extreme limits. In the one, represented by the dashed lines, the target radius is taken to be infinite so that $\delta\psi_0$ is replaced by a planar cut-off. In the other, shown as full-drawn lines, the target radius R_a is assumed small, so that the wave function is replaced by its value along the axis $(b,0,z)$ of the target trajectory seen from the halo's coordinate system. The two approximations, which for the case of neutrons both lead to convenient analytical expressions [2], are seen to agree well. The strong dependence on impact parameter arises from localization of the wave function in the direction perpendicular to the beam; the effect would not be present for a wave function that factorizes in cylindrical coordinates such as a plane wave or a Gaussian, which may explain why it was not considered initially.

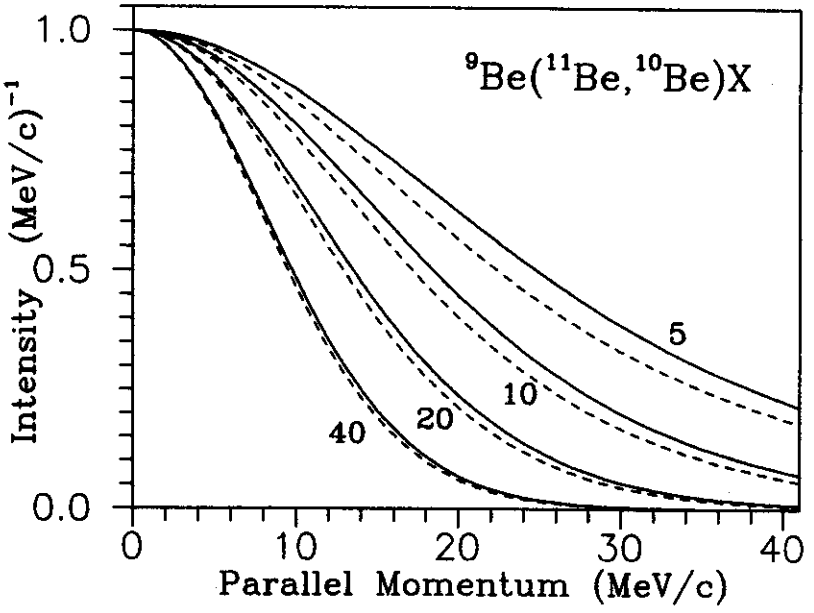

Fig. 1: Parallel momentum distributions calculated for the case of ^{11}Be neutron halo ($s_{1/2}$ ground state, S_n=0.504 MeV) incident on a beryllium target and for a beam energy of 63 MeV/u. Normalized to unity at the origin, the four pairs of curves correspond to fixed impact parameters of 5, 10, 20, and 40 fm. The full drawn curves are the cylindrical approximation and the dashed ones the planar cut-off approximation.

The differential cross sections can now be obtained by integrating over impact parameter to give for l=0

$$\frac{d\sigma_o}{dk_z} = \frac{\sigma_T B^2 \kappa b_{\min}^2}{2\pi}\left[K_1^2 - K_0^2\right]$$

and for l=1

$$\frac{d\sigma_1}{dk_z} = \frac{\sigma_T B b_{\min}^2}{2\pi\kappa}\left[k(K-K)+(k+\kappa)\left(K_2^2 - K_1^2 - \frac{2}{\xi}K_1 K\right)\right]$$

where the argument of the modified Bessel functions is understood to be $\xi = b_{min}\,(\kappa^2+k_z^2)^{1/2}$. Here $\kappa=(2\mu S_n)^{1/2}/\hbar$ determined in terms of the reduced mass and neutron separation energy. The dimensionless constant B, of order unity, is determined by joining the outer and inner solutions to the Schrödinger equation. The single-nucleon stripping cross sections are obtained by integrating over the parallel wave vector k_z. Results obtained with these two expressions are shown in Figs. 2 and 3. The quantity σ_T is the experimentally determined total nucleon cross section.

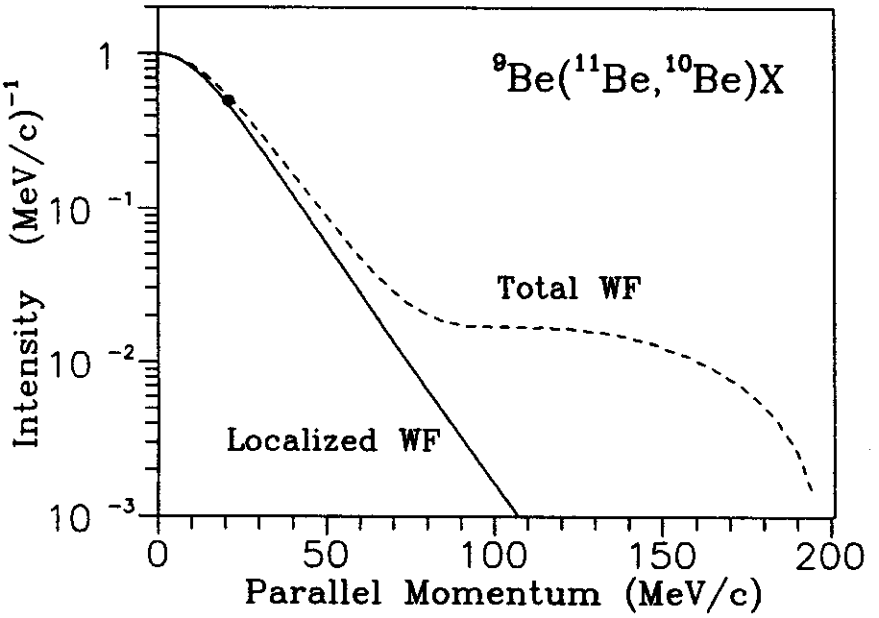

Fig. 2: Parallel momentum distribution of the cross section (full drawn) calculated for the case of ^{11}Be. The dashed curve is the momentum distribution of the total wave function. The dot represents the measured half width at half maximum.

The corresponding momentum distributions for halo protons were calculated numerically with a Woods-Saxon single-particle wave functions very similar to those used by Brown et al. [1]. These were also used for estimating B and for calculating the momentum distributions of the total wave function shown in Figs. 2 and 3. For neutrons, the parallel-momentum distributions obtained in a numerical calculation were in essentially exact agreement with the analytical expressions given above.

Fig. 2 shows that for the case of ^{11}Be there is good agreement between the experimental parallel momentum width [3] and the calculation. The distribution corresponding to the total wave function has a very similar width; in view of the strong dependence on impact parameter shown in Fig. 1, this can be considered as a numerical coincidence. This is underscored by the fact that the plateau around 150 MeV/c is entirely absent in the momentum distribution of the localized wave function. To see why this is so, we note that the high momentum components in the wave function in momentum space are the counterpart of the inner lobe peaking at 0.7 fm in the spatial wave function. In the approximation used here, this is a region of space that is not sampled in the experiment.

For the case of ^{8}B, the full width at half maximum characterizing the momentum distribution of the total wave function, 153 MeV/c, is very much broader than the calculated value of 75 MeV/c, which agrees well with the experimental value of 81±6 MeV/c. The apparent discrepancy between the widths of the total momentum distribution and that of the experiment originally led to the claim [4] that an

interpretation in terms of single particle model was not possible. The calculation for ^{8}B omitting the Coulomb force shows that very similar results would be obtained for a p state halo neutron.

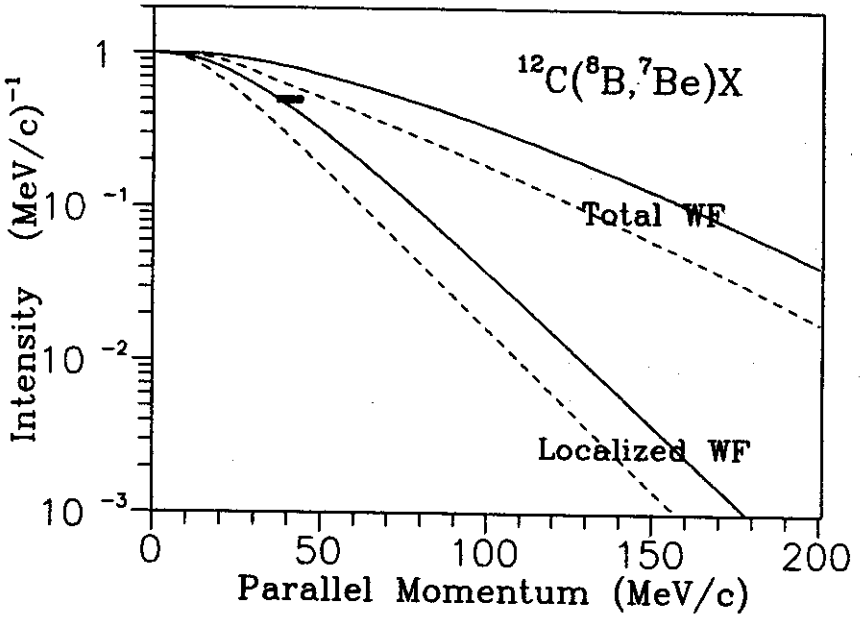

Fig. 3: Parallel momentum distributions (full drawn) calculated for the case of the ^{8}B proton halo ($p_{1/2}$ ground state, S_p=0.137 MeV) incident on a beryllium target and for a beam energy of 1471 MeV/u. The bar represents the measured half width at half maximum [4]. The dashed curves show the results of neglecting the Coulomb interaction between the proton and the ^{7}Be core.

An independent verification of the estimates given here is provided by the measured cross sections. The calculated ^{11}Be cross section of 316 mb at 41 MeV/u is roughly one third of the free-nucleon value and agrees well with the experimental value [6] of 290±40 mb. The ^{8}B cross sections are calculated as 111 mb at 40 MeV/u and 54 mb at 1471 MeV/u are roughly one tenth of the free-nucleon values and are qualitatively in good agreement with the measured [7,4] values of 80±15 and 94±4 mb, respectively. The overall agreement must be considered satisfactory, but it is probably worth noting that the tendency of the model with the cylindrical reaction zone must be to underestimate the cross sections and widths, and most so for the case of ^{8}B, which the external wave function falls off rapidly.

The interpretation given here has an important implication for the analysis of experimental data, namely that, contrary to what is often assumed, the longitudinal momentum distributions measured with a light target should not be affected appreciably by the acceptance of the spectrometer. Basically, this may be seen from the uncertainty principle, which allows an exact measurement of the momentum along the z-axis for a precisely known (x,y) coordinate. For an infinitesimal target it follows that all information about the original momentum in the xy plane will be destroyed by the measurement. For a small target the radial momentum distribution of the neutron in the approximation leading to the expressions above becomes proportional to $[J_1(k_r R_a)/k_r R_a]^2$, the usual diffraction pattern, depending only on the radius of the target. This means that the wave function at the moment of the collision takes a form that factorizes, see the comments above, so that the k_z distribution will not be changed by an incomplete detection of the k_x and k_y components.

To sum up, the parallel momentum of the heavy fragment in processes such as (^{11}Be,^{10}Be) and (^{8}B,^{7}Be) on light targets reflects the halo wave function in a localized region outside of the nuclear core.

When this is taken into account, the calculated longitudinal momentum widths and reaction cross sections are in good agreement with the experiments. The measured widths are shown to be insensitive to the transverse acceptance of the spectrometer. The transverse momentum components and also the momentum distributions of the halo nucleon(s) should give interesting complementary information, see [8].

References

1. B.A. Brown, A. Csótó and R. Sherr, Nucl. Phys A **597**, 66 (1996).
2. P.G. Hansen, Proc. Int. Conf. Exotic Nuclei and Atomic Masses (ENAM), Arles June 1995 (D. Guillemaud-Mueller ed.) 1995, in press, and to be published.
3. J.H. Kelley et al., Phys. Rev. Lett. **74**, 30 (1995).
4. W. Schwab et al., Z. Phys. A **350**, 283 (1995).
5. Sam M. Austin et al., personal communication, to be published.
6. R.Anne et al., Nucl. Phys. A **575**, 125 (1994); Phys. Lett B **304**, 55 (1993).
7. I. Pecina et al., Phys. Rev. C **52**, 191 (1995)
8. P.G. Hansen, A.S. Jensen and B. Jonson, Nuclear Halos, Ann. Rev. Nucl. Part. Sci. **45**, 591 (1995).

NEUTRON HALOS IN THE Na ISOTOPES

B.A. Brown and W.A. Richter[a]

Recent experimental results have been reported for the matter radii of the neutron-rich Na isotopes based upon a Glauber-model analysis of interaction cross-section data [1]. Comparison of these results with estimates of the charge radii [2] provides one of the best examples of neutron skin behaviour for an extended series of isotopes. It also brings back into interest the long standing observation of the vanishing of the N=20 shell closure for ^{32}Mg and nearby nuclei. In this work we use the Hartree-Fock model with the SGII Skyrme interaction [3] to study the proton and neutron density distributions, and we also discuss some of the special shell-model features of the most neutron-rich Na isotopes which are important for determining the location of the drip line.

The SGII Skyrme interaction has been used previously both for global charge radii comparisons [4] as well as for the neutron halos of light nuclei [5]. The neutron rms radii obtained with SGII are compared with the experimental range of values deduced in [1] in Fig. 1. The solid line is the SGII HF results obtained when the spherical orbitals are occupied sequentially in the order given by the HF potential, namely: $0d_{5/2}$, $1s_{1/2}$, $0d_{3/2}$, $0f_{7/2}$, $1p_{3/2}$ and $1p_{1/2}$. (For the closed-shell configurations such as N=20, these calculations correspond directly to the exact HF equations. For the open-shell configuration the potential is approximated by the spherical potential obtained by weighting the radial density profile for a given orbital by its occupation probability.) At $N = 34$ the next orbital, $0f_{5/2}$, is unbound and the drip line is reached. For the sd-shell nuclei ($N = 9 - 20$) we also show the SGII HF results (crosses) obtained with the fractional orbital occupancies calculated from the Brown-Wildenthal sd-shell wave functions [6]. The SGII HF results are close to the RMF calculation shown in [1] up to $N = 15$, but for $N = 16 - 19$ the RMF values lie somewhat higher than our calculation and also outside the experimental errors. The experimental dip around $N = 11$ is not explained by either calculation. The results for the proton rms radii are also shown in Fig. 1. Both the RMF and present calculations are in reasonable agreement with experiment. It is remarkable how little the proton radii change compared to the increasing neutron radii, so that by $N = 21$ a significant neutron skin appears.

We can also compare directly with the interaction cross section data[1], by using our densities to calculate the Glauber-model cross sections, as was done for light nuclei in [5]. The results with the zero-range interaction are shown in Fig. 2. The calculations are in excellent agreement with experiment. It is interesting to note the change in calculated slope at the semi-magic numbers $N = 14$ and $N = 28$, with the change at $N = 14$ also appearing in the data. Changes in the experimental charge-radii differences also appear at $N = 14$ and $N = 28$ [4].

The rather large neutron skin for the neutron-rich Na isotopes is in contrast to the situation near the line of maximum stability for nuclei such as ^{208}Pb [7,8], where the proton and neutron radii are nearly equal even when N/Z is relatively large. Since the potential well for protons is determined mainly by the neutron density, the proton potential becomes larger in radius as a function of increasing neutron number, and thus one may think that the proton radius should also increase. However, the potential for protons also becomes deeper as a function of increasing neutron number and this tends to counteract the effect of the radial size increase. The difference between the proton and neutron potentials manifests itself in a difference between the Fermi energies for protons and neutrons (as observed in the proton and neutron separation energies). In ^{31}Na the Fermi energy for protons is about 12 MeV larger than that for neutrons,

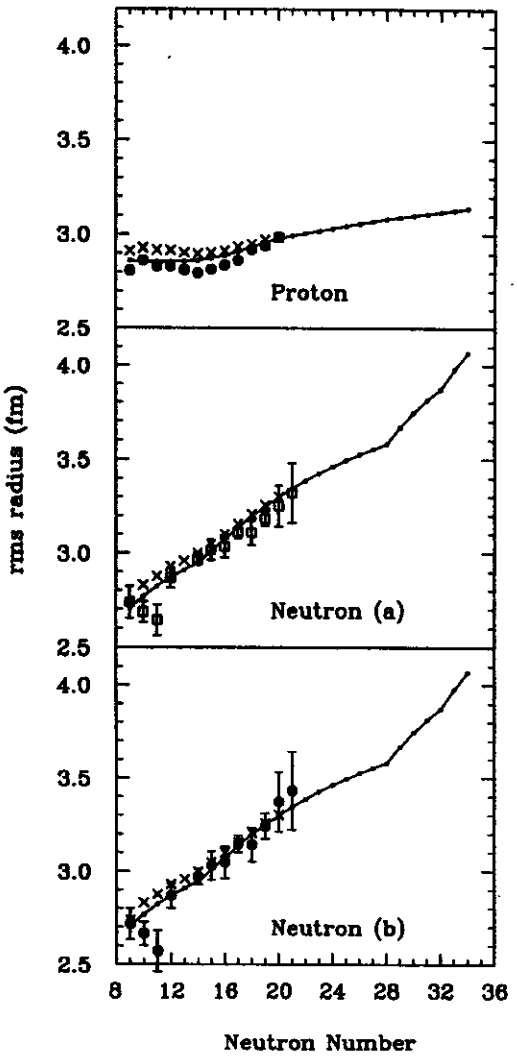

Figure 1: Calculated and measured proton and neutron rms radii as a function of neutron number of the Na isotopes. The calculations were based on the SGII Skyrme parameterization. The small dots and solid line correspond to the HF calculation with simple occupation numbers, and the crosses were obtained with the sd-shell occupation numbers. The solid points in the top panel are the experimental proton rms radii. The points with error bars in middle and bottom panels correspond to the experimental neutron rms radii obtained with assumptions (a) and (b), respectively, from [1].

in contrast to the situation in a nucleus such as ^{208}Pb where the proton and neutron Fermi energies are about equal to each other. The situation for ^{48}Ca is intermediate to that of ^{31}Na and ^{208}Pb with a proton-neutron rms radius difference of $0.1 - 0.2$ fm [9,10] and 6 MeV difference in the Fermi energies.

The spherical HF calculations for $N = 20$ presented in Fig. 1 have a closed sd-shell configuration. However, it has long been known experimentally that the $N = 20$ is not a good closed shell for ^{32}Mg and nearby nuclei. This information comes from the binding energy systematics [11,12], from the low-lying 2^+ energy in ^{32}Mg [13] and its large B(E2) value [20], and from the beta decay [14]. The increase in the Na proton radii between $N = 15$ and $N = 20$ may be another indication of the deformation at $N = 20$. Theoretically, this deformation has been understood from deformed HF calculations [15] and well as configuration mixed shell-model calculations [16,17,18]. The shell-model approach provides the most detail in terms of excited state energies and wave functions. The shell-model calculation for ^{31}Na of [16] indicates that the $2\hbar\omega$ intruder configuration with two neutrons excited from the sd to the fp shell lies

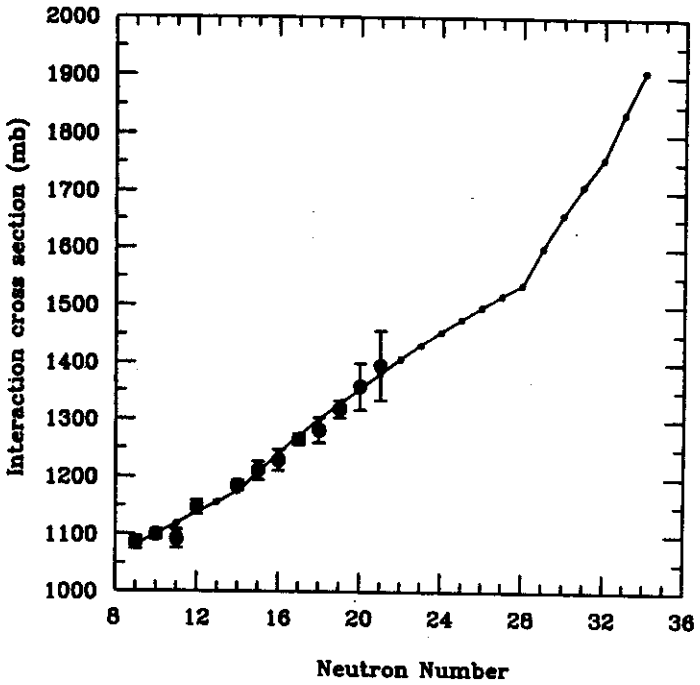

Figure 2: Calculated Glauber interaction cross sections obtained with the zero-range interaction of [5] (solid line) compared with the experimental data [1] (filled circles with error bars).

lower in energy than the closed sd shell configuration. It appears from the shell-model calculations that the intruder states are isolated to a region around ^{32}Mg and for this reason it has been referred to as an "island of inversion". A similar inversion for the ground state ^{11}Be ground state is well known and can also be understood from shell-model calculations [19].

We assume that beyond a neutron number of $N = 23$ that the configurations become spherical again, and that it thus makes sense to use the ordering of level occupancies obtained in the spherical Hartree-Fock calculations. But this has yet to be confirmed experimentally. The spherical calculations are continued in Figs. 1 and 2 out to the drip line. The proton radii remain relatively flat and the neutron radii (and the interaction cross sections) increase more rapidly as the $N = 34$ drip line is reached. The more rapid increase corresponds to the change from the filling of the $0f_{7/2}$ orbital to the 1p orbitals which have a smaller angular momentum barrier and smaller separation energies and thus a large rms radius.

The position of the neutron drip line is primarily determined by the valence neutron single-particle energies (SPE). The SGII neutron SPE for the most neutron-rich Na isotopes are shown in Fig. 3. One observes an overall decrease in their energy, but when $N = 34$ is reached the next orbital, $0f_{5/2}$, is unbound and thus $N = 35$ is not stable. What is important in Fig. 3 are the absolute neutron SPE at $N = 20$ and their slope as a function of neutron number. The SGII interaction systematically underbinds the valence particle states in light nuclei; for example, the ^{16}O $0d_{5/2}$ experimental (SGII) SPE is -4.14 (-7.05) MeV and the ^{40}Ca $0f_{7/2}$ SPE is -8.36 (-9.70) MeV. Thus, we must assume that the SPE for the neutron-rich Na isotopes obtained with SGII are also too bound by about 2.5 MeV. Qualitatively this would shift all of the points in Fig. 3 up by about this amount. This means that all of the Na isotopes are on the very edge of being bound and that the non-monpole correlation energies as well as the intruder states energies will be the determining factor in the location of the drip line.

Assuming an $N = 20$ closed shell, the shell-model result [16] for the ^{32}Na energy minus the ^{31}Na

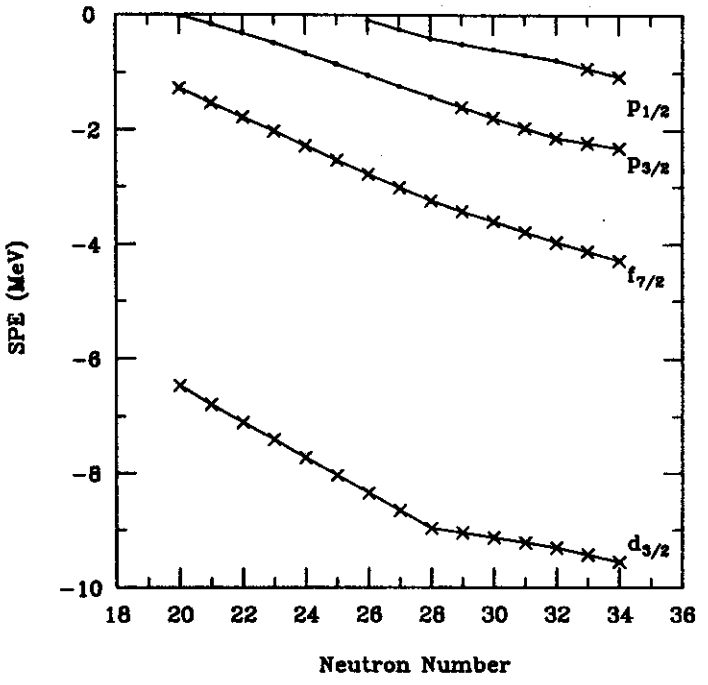

Figure 3: Single-particle energies (SPE) of the Na isotopes as a function of neutron number, using the SGII Skyrme parameterization. A cross indicates the order in which the orbital are occupied as a function of neutron number.

energy is -0.56 MeV. This energy difference can be decomposed into $+1.12$ MeV coming from the (unbound) monopole $0f_{7/2}$ SPE plus -1.67 MeV correlation energy. When the intruder states are included, the ground state of ^{31}Na has a two-particle two-hole ($2p-2h$) configuration (Fig. 4 of [16]), the ground state of ^{32}Na has a $2p-1h$ configuration (Fig. 5 of [16]), and the energy difference is -1.14 MeV. The experimental value [21] is $-2.4(5)$ MeV. Again, assuming an $N=20$ closed shell, the shell-model result for the ^{33}Na energy minus the ^{31}Na energy is -4.1 MeV which can be approximately decomposed into $+2.2$ MeV from the SPE, -3.9 MeV from neutron-neutron pairing and -2.4 MeV from the proton-neutron correlations. The experimental value [21] is $-3.3(15)$ MeV. (The calculated change due to intruder states is small.) Thus the correlation energy calculations will be important for determinig the properties of all neutron-rich Na isotopes, but they are beyond the scope of the present work. Similar comments apply to the Ne isotopes, where we note that ^{32}Ne [22] and ^{31}Ne [23] are both stable, but the masses have not yet been measured.

a. Department of Physics, University of Stellenbosch, Stellenbosch 7600, South Africa

References

1. T. Suzuki et al., Phys. Rev. Lett. 75, 3241 (1995)
2. G. Huber, F. Touchard, S. Büttgenbach, C. Thibault, R. Klapisch, H. T. Duong, S. Liberman, J. Pinard, J.L. Vialle, P. Juncar, and P. Jacquinot, Phys. Rev. C18, 2342 (1978).
3. N. van Giai and H. Sagawa, Nucl. Phys. A371, 1 (1981), N. van Giai and H. Sagawa, Phys. Lett. B106, 379 (1981)
4. B. A. Brown, C. R. Bronk and P. E. Hodgson, J. Phys. G10, 1683 (1984).
5. G. F. Bertsch, B. A. Brown and H. Sagawa, Phys. Rev. C39, 1154 (1989).
6. B. A. Brown and B. H. Wildenthal, Annu. Rev. Nucl. Sci. 38, 29 (1988).
7. B. A. Brown, S. E. Massen, J. I. Escudero, P. E. Hodgson, G. Maduga and J. Vinas, J. Phys. G9, 423 (1983).

8. C. J. Batty, E. Friedman, H. J. Gils and H. Rebel, Adv. Nucl. Phys. 19, 1 (1989).
9. B. A. Brown, S. E. Massen and P. E. Hodgson, J. Phys. 5, 1655 (1979).
10. W. R. Gibbs and J. P. Dedonder, Phys. Rev. C46, 1825 (1992).
11. C. Thibault, R. Klapisch, C. Rigaud, A. M. Poskanzer, R. Prieels, L. Lessard and W. Reisdorf, Phys. Rev. C12, 644 (1975).
12. B. H. Wildenthal and W. Chung, Phys. Rev. C22, 2260 (1980).
13. C. Detraz, D. Guillemaud, G. Huber, R. Klapisch, M. Langevin, F. Naulin, C. Thibault, L. C. Carraz and F. Touchard, Phys. Rev. C19, 164 (1979).
14. B. H. Wildenthal, M. S. Curtin and B. A. Brown, Phys. Rev. C28, 1343 (1983).
15. X. Campi, H. Flocard, A. K. Kerman and S. Koonin, Nucl. Phys. A251, 193 (1975).
16. E. K. Warburton, J. A. Becker and B. A. Brown, Phys. Rev. C41, 1147 (1990).
17. A. Poves and J. Retamosa, Phys. Lett. B184, 311 (1987); Nucl. Phys. A571, 221 (1994).
18. N. Fukunishi, T. Otsuka and T. Sebe, Phys. Lett. B296, 279 (1992).
19. H. Esbensen, B. A. Brown and H. Sagawa, Phys. Rev. C51, 1274 (1995)
20. T. Motobayashi et al., Phys. Lett. B346, 9 (1995).
21. G. Audi and A. H. Wapstra, Nucl. Phys. A595, 409 (1995).
22. D. Guillemaud-Mueller et al., Phys. Rev. C41, 937 (1990).
23. I. Tanihata, private communication.

SHELL-MODEL PROPERTIES OF ^{11}Li

B. A. Brown

The properties of ^{11}Li present a challenge to the conventional shell-model approach, [1] because of the very loose binding of the last two neutrons. It is important to explore the conventional approach in order to see where it breaks down and how it can be improved. In this note I investigate the β decay properties of ^{11}Li from the point of view of the conventional 0p shell model and its extension to include effects from "intruder" 1s0d shell configurations. I also comment on the properties of some low-lying excited states of ^{11}Li.

The 0p model-space allows for all possible mixing between the $0p_{3/2}$ and $0p_{1/2}$ orbital configurations. In Fig. 1 the ^{11}Li to ^{11}Be β^- B(GT) values summed as a function of excitation energy are shown for three

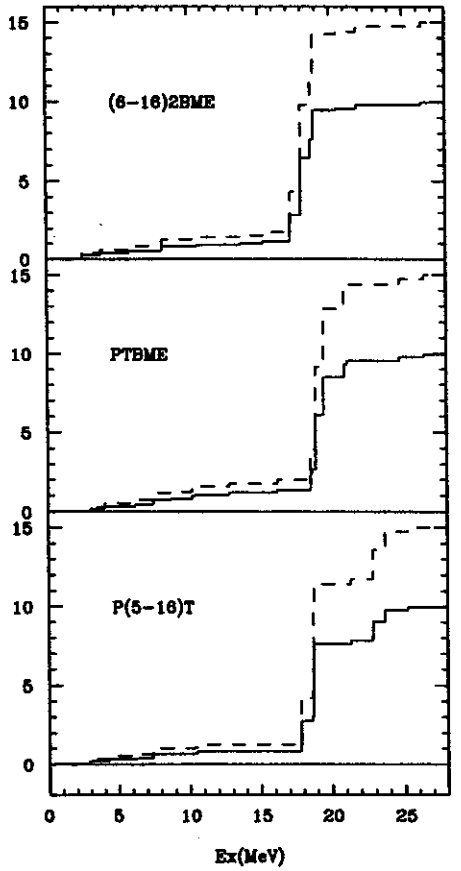

Figure 1: Total GT strength obtained with the three 0p-shell interactions discussed in the text. The strength is shown as a running sum of the excitation energy. The dashed line is with the free-nucleon GT operator and the solid line is with the effective (renormalized) GT operator.

different effective interactions. The dashed lines correspond to the free-nucleon Gamow-Teller operator. Since the β^+ strength is zero in the 0p shell model, the sum rule of 3(N-Z)=15 applies to the β^- strength and is common to all calculations. As in the 1s0d shell, [2] the experimental GT strengths for 0p shell nuclei are systematically reduced (quenched) relative to the free-nucleon operator calculations. The effective GT operator obtained from a fit to experiment (the operator from the bottom left of Table IV in Ref 3) has

been used to obtain the results shown by solid lines in Fig. 1. The matrix elements obtained from the effective operator are reduced from the free-nucleon values by a factor of about 0.815 and the GT strength is reduced by a factor of about 0.66. The sum rule is, therefore, reduced to about 10.0. This reduction is due to higher-order nucleon configuration mixing (beyond the 0p shell) and delta admixtures. [4]

I have chosen three representative 0p shell interactions which have been obtained from analyses of global 0p-shell energy-level data. The (6-16)2BME interaction of Cohen and Kurath [5] was obtained from a least squares fit of two-body Hamiltonian matrix elements to the energy-level data as it was known in 1965. More recent 0p-shell energy-level data was taken into account in the two-body matrix-element fit of Julies, Richter and Brown, [6] and the GT distribution obtained with this interaction (PTBME) is shown in the middle of Fig. 1. Finally, I show the distribution calculated with the P(5-16)T interaction.[7]

All three calculations show a similar pattern. There are four types of neutron to proton components to the GT decay amplitude: (a) a low-lying $0p_{1/2}$ to $0p_{3/2}$ transition, (b) a medium-energy $0p_{3/2}$ to $0p_{3/2}$ transition, (c) a medium energy $0p_{1/2}$ to $0p_{1/2}$ transition, and (d) a high-energy $0p_{3/2}$ to $0p_{1/2}$ transition. These mix, resulting in a low-energy region below 15 MeV where (a) dominates but is partially cancelled by smaller admixtures (b), (c) and (d), and a narrow giant GT resonance region around 17 MeV in excitation energy where all amplitudes are in phase. Recent experiments at the NSCL [8] indicate that the GT strength up to about 10 MeV in excitation energy in ^{11}Be is smaller than the renormalized results shown in Fig. 1 (solid lines) by about a factor of two.

None of the above calculations explicitly takes into account the halo nature of ^{11}Li. Three effects may be important: (1) The overall strength of the transition components which start with a $0p_{1/2}$ neutron should be reduced since the large radial extent of the $0p_{1/2}$ neutron gives a reduced radial overlap with the more tightly bound 0p protons. (2) Since the $1s_{1/2}$ neutron orbital is the ground state of ^{11}Be, the last two neutrons in ^{11}Li are expected to have some $(1s0d)^2$ admixture. This component has no overlap with the final states and hence serves as another source of reduction. (3) The quenching factor applied to the above calculations may be smaller (closer to unity) for the "free" neutrons in the halo.

All of these effects lead to modifications of the $0p_{1/2}$ neutron contributions (a) and (c) relative to the $0p_{3/2}$ contributions (b) and (d). Thus I investigate what happens to the GT strength when components (a) and (c) are modified by an overall factor between 0.0 and 1.0. The results are shown in Fig. 2. I have chosen to make this comparison with the Cohen-Kurath (6-16)2BME interaction because it gives best agreement (again with the renormalized operator) for the low-lying decay[9] of ^{9}Li, which is the core of the two loosely bound neutrons in ^{11}Li. (The conclusions are similar with the other two interactions.) The behaviour seen in Fig. 2 is due to the cancellation between the (a) and (b,c,d) components of the transition amplitude. The cancellation is maximized with a reduction factor of about 0.5 below which (a) begins to dominate.

Optimal agreement is obtained for two values of the $0p_{1/2}$ reduction factor – values of about 0.30 and 0.80, with the shape of the GT distribution being somewhat better reproduced with the value of 0.8. To take into account effect (3), one can consider the extreme in which the global factor of 0.815 discussed above is removed for components (a) and (c). The reduction factors then become 0.24 and 0.65, respectively.

Now I discuss the estimates for the radial overlap and 1s0d mixing effects mentioned above. Using Woods-Saxon wave functions and fixing the binding energy of the valence neutron to the range of values 0.3-0.7 MeV, the calculated neutron $0p_{1/2}$ and proton 0p radial overlap is 0.81 to 0.85.

Shell-model calculations for ^{11}Li in a 0+2 $\hbar\omega$ model space have recently been carried out.[10] The energies of the lowest unmixed $0\hbar\omega$ and $2\hbar\omega$ $3/2^-$, T=5/2 wavefunctions are nearly degenerate. Mixing

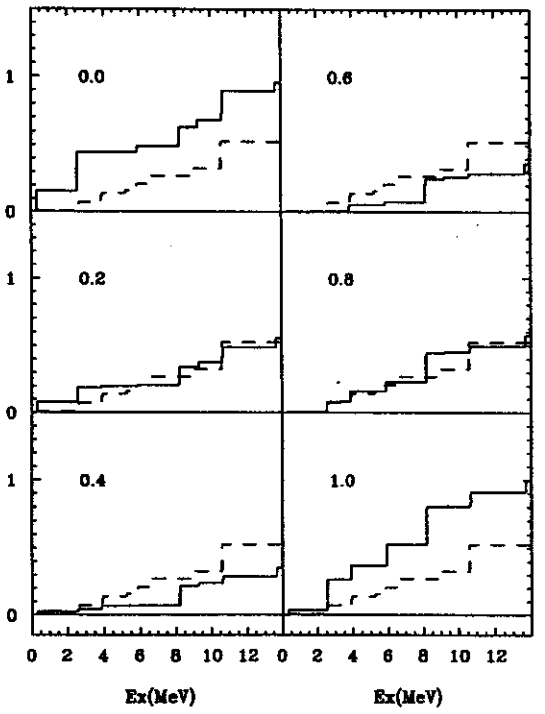

Figure 2: Low-lying GT strength from the (6-16)TBME calculation as a function of the $0p_{1/2}$ reduction factor (solid lines) compared with experiment (dashed lines).

these with the "shift method" and WBT interaction discussed in results[11] in a wave function for the ^{11}Li ground state which has 56 percent $0\hbar\omega$ and 44 percent $2\hbar\omega$ and neutron occupation numbers of 3.69, 1.45, 0.39, 0.07 and 0.39 for the $0p_{3/2}$, $0p_{1/2}$, $0d_{5/2}$, $0d_{3/2}$ and $1s_{1/2}$ orbitals, respectively. The occupation factor for the $0p_{1/2}$ orbital is thus $(1.45/2)^{1/2}$=0.85. Combining this occupation factor with the overlap factor discussed above would give a total $0p_{1/2}$ reduction factor of 0.69 to 0.72, which is consistent with the range of values 0.65 (no global quenching) to 0.80 (0.815 global quenching) obtained empirically.

One could calculate the ^{11}Li beta decay directly with the 0+2 $\hbar\omega$ wave functions. However, since the WBT interaction uses a 0p shell interaction which is essentially the same as the pure 0p shell interactions used above, the effect of the $2\hbar\omega$ admixtures is to incorrectly renormalize this 0p interaction. Although the gross properties of the 0+2 $\hbar\omega$ wave functions such as the amount of $2\hbar\omega$ admixture and the occupation numbers are probably reasonable, the detailed properties of the 0+2 $\hbar\omega$ wave functions which are needed for the β decay calculations are less accurate than the $0\hbar\omega$ 0p shell wave functions. Before a direct 0+2 $\hbar\omega$ calculation for the β decay can be carried out the 0p interaction must be modified. In addition the effects of radial overlap and global renormalization (as included in the analysis above) must be included.

Suzuki and Otsuka have considered the effect of the neutron halo on the GT transition strength to the 0.32 MeV $3/2^-$ level in ^{11}Be. This particular transition is, however, only 0.06 percent of the sum rule value 3(N-Z)=15, and is thus very sensitive to all aspects of the calculation, in particular, the 0p Hamiltonian. The total transition strength to all low-lying states up to about 10 MeV as observed in the NSCL experiment[8] is a much less model-dependent measure of the neutron halo properties.

The total calculated GT strength in the giant resonance region is about 9. It would be interesting

to obtain better data for the higher energy region perhaps from inverse reactions with radioactive beams. The position of the IAS is 21.86, 21.13 and 21.31 MeV with the (6-16)2BME, PTBME and P(5-16)T interactions, respectively. In all cases the IAS contains the usual (N-Z)=3 Fermi strength but only a very little GT strength. Most of the giant GT strength is predicted to lie below the IAS.

The WBT interaction was designed to reproduce the $1\hbar\omega$ parity inversion of the ^{11}Be ground state.[12] When the WBT interaction is applied to the pure $N\hbar\omega$ configurations of the N=8 isotones, the pure $1\hbar\omega$ excitations always lie several MeV above the ground state – there is no parity inversion. However, it is remarkable to find that the $2\hbar\omega$ excitations which start out at 9 MeV in ^{16}O quickly come down in energy (8 MeV in ^{15}N, 5 MeV in ^{14}C and 3 MeV in ^{13}B) until they become essentially degenerate with the $0\hbar\omega$ configuration in ^{12}Be, ^{11}Li and ^{10}He. When the $0\hbar\omega$ and $2\hbar\omega$ configurations are allowed to mix in these three nuclei, there are (as mentioned above for ^{11}Li) two states each with about 50-50 admixture of $0\hbar\omega$ and $2\hbar\omega$.

Barker [13] has pointed out the possibility for a mixed $(0+2)\hbar\omega$ configuration for the ^{12}Be ground state. One of the most direct radioactive beam experiments which would test the structure of the ^{12}Be ground state is the pick-up of one neutron leading to the $1/2^{\pm}$ parity doublet in ^{11}Be (with a resolution capable of separating the 0.32 MeV doublet). A pure $0\hbar\omega$ configuration would lead only to the $1/2^-$ final state, whereas the mixed configuration will also lead to the $1/2^+$ final state (the calculated spectroscopic factor is about 0.4).

The mixed $0+2$ $\hbar\omega$ wave functions lead to low-lying excited states in ^{12}Be, ^{11}Li and ^{10}He which have the same spin and parity as the ground states. The excitation energies of these states depend upon the $< 0p, 0p \mid V \mid 1s0d, 1s0d >$ off-diagonal interaction. With the WBT interaction the excitation energy is 1.2-1.4 MeV for ^{10}He, ^{11}Li and ^{12}Be. When the Bonn (WBN) interaction is used [14] the excitation energy goes up to 2.2-2.7 MeV. There is a state [15] at 2.70 MeV in ^{12}Be which is presumably 0^+ and is close to the WBN calculation. There are several candidates for low-lying states in ^{11}Li.[16] The calculated inelastic scattering amplitudes between the ground state and excited states in these three nuclei have a strong $1s_{1/2}$ to $0p_{1/2}$ monopole component, and the calculated angular distributions may help to make a correspondence between experiment and theory.

References

1. B. A. Brown and B. H. Wildenthal, Annu. Rev. Nucl. Sci. 38, 29 (1988).
2. B. A. Brown and B. H. Wildenthal, At. Data Nucl. Data Tables, 33, 347 (1985).
3. W. T. Chou, E. K. Warburton and B. A. Brown, Phys. Rev. C47, 163 (1993).
4. B. A. Brown and B. H. Wildenthal, Nucl. Phys. A474, 290 (1987).
5. S. Cohen and D. Kurath, Nucl. Phys. 73, 1 (1965).
6. R. E. Julies, W. A. Richter and B. A. Brown, South African Jour. Phys. 15, 45 (1992).
7. E. K. Warburton and B. A. Brown, Phys. Rev. C46, 923 (1992).
8. D. J. Morrissey et al., unpublished.
9. D. Mikolas et al., Phys. Rev. C37, 766 (1988).
10. B. A. Brown in the International Conference on Exotic Nuclei and Atomic Masses, Arles, France, June 19-23, 1995, to be published.
11. E. K. Warburton, B. A. Brown and D. J. Millener, Phys. Lett. B293, 12
12. H. Sagawa, B. A. Brown and H. Esbensen, Phys. Lett. B309, 1 (1993).
13. F. C. Barker, J. Phys. G2, L45 (1976).
14. E. K. Warburton, I. S. Towner and B. A. Brown, Phys. Rev. C49, 824 (1994).
15. H. T. Fortune, G. B. Liu and D. E. Alburger, Phys. Rev. C50, 1355 (1994).
16. A. A. Korsheninnikov et al., Phys. Rev. C53, R537 (1996).

LOW-ENERGY M1 STRENGTH IN THE ^{7}Li$(p,\gamma_0)^8$Be REACTION

Attila Csótó[a] and Steven Karataglidis

Astrophysical processes most often involve charged particle nuclear reactions at very low energies. The cross sections of such reactions decrease exponentially with decreasing energy, making their laboratory measurements extremely difficult. One of the most important reactions in nuclear astrophysics is the radiative proton capture on ^{7}Be. This reaction produces ^{8}B in the Sun, whose β^+ decay is the main source of high-energy solar neutrinos. That ^{7}Be is radioactive makes the measurement of the low-energy ^{7}Be$(p,\gamma)^8$B cross section even more difficult. The cross section at low energies ($E < 200$ keV) is dominated by the $E1$ transition and so the extrapolated astrophysical S factor is flat.

Herein, we study the role of the $M1$ transition in the ^{7}Li$(p,\gamma)^8$Be reaction. This reaction has been the subject of much investigation [1–6] as the somewhat easier experimental situation (^{7}Li is stable) might allow one to gain some insight into the similar ^{7}Be$(p,\gamma)^8$B process. However, there is some disagreement as to the strength of the $M1$ contribution to the low-energy cross section, affecting the $E1$ strength at low energies, with estimates varying from 6% [5] to 20% [1].

Our model is a microscopic multi-cluster (^{4}He+^{3}H+p; ^{4}He+^{3}He+n; α+α) Resonating Group Method (RGM) approach to the eight-nucleon system. The trial function of the eight-body system is

$$\begin{aligned}\Psi &= \sum_{S,l_1,l_2,L} \mathcal{A}\left\{\left[\left[\Phi^p(\Phi^\alpha\Phi^t)\right]_S \chi_{[l_1l_2]L}(\rho_1,\rho_2)\right]_{JM}\right\} \\ &+ \sum_{S,l_1,l_2,L} \mathcal{A}\left\{\left[\left[\Phi^n(\Phi^\alpha\Phi^h)\right]_S \chi_{[l_1l_2]L}(\rho_1,\rho_2)\right]_{JM}\right\} \\ &+ \mathcal{A}\left\{\left[\Phi^\alpha\Phi^\alpha\chi_L(\rho)\right]_{JM}\right\}, \end{aligned} \tag{1}$$

where $\mathcal{A}$ is the intercluster antisymmetrizer, the Φ cluster internal states are translationally invariant harmonic oscillator shell model states ($\alpha = {}^4$He, $t = {}^3$H, and $h = {}^3$He), the ρ vectors are the different intercluster Jacobi coordinates, l_1 and l_2 are the angular momenta of the two relative motions, L and S are the total orbital angular momentum and spin, respectively, and [...] denotes angular momentum coupling. The sum over S, l_1, l_2, and L includes all physically relevant angular momentum configurations. In order to project out pure ^{7}Li and ^{7}Be states, the angular momenta are recoupled in the 7+1 channels following the scheme

$$\left[(l_1,l_2)L,(s_1,s_2)S\right]J \rightarrow \left[\left[(l_1,s_1)I_7,s_2\right]I,l_2\right]J, \tag{2}$$

where I_7 is the total spin of the seven nucleon system, and I is the channel spin.

The ^{7}Li$(p,\gamma_0)^8$Be radiative capture cross section is calculated perturbatively [7], and is given by

$$\begin{aligned}\sigma &= \sum_{\Omega,\lambda} \frac{1}{(2I_7+1)(2s_2+1)} \frac{8\pi(\lambda+1)}{\hbar\lambda(2\lambda+1)!!}\left(\frac{E_\gamma}{\hbar c}\right)^{2\lambda+1} \\ &\times \sum_{l_\omega,I_\omega} (2l_\omega+1)^{-1} |\langle \Psi^{J_f} || \mathcal{M}^\Omega_\lambda || \Psi^{J_i}_{l_\omega,I_\omega}\rangle|^2, \end{aligned} \tag{3}$$

where I_7 and s_2 are the spins of the colliding clusters, λ denotes the rank of the electromagnetic operator $\mathcal{M}^{\Omega}_{\lambda}$ ($\Omega = E$ or M), ω represents the entrance channel, and J_f and J_i is the total spin of the final and initial state, respectively. The initial wave function $\Psi^{J_i}_{l_\omega,I_\omega}$ is a partial wave of a unit-flux scattering wave function.

The final ^{8}Be ground state is unbound in the $\alpha + \alpha$ channel which, in principle, could cause convergence problems. However, this is not the case here since the ^{7}Li+p and ^{7}Be+n channel wave functions are orthogonal to the $\alpha + \alpha$ one in the asymptotic spatial region. This feature allows us to treat the ^{8}Be ground state as a pseudo-bound state in the $\alpha + \alpha$ configuration. The orthogonality also indicates that the ^{7}Li+$p \rightarrow \alpha + \alpha$ contribution to the cross section is small, and that the inclusion of the $7 + 1$ configurations in the ^{8}Be ground state is important.

Putting (1) into the eight-nucleon Schrödinger equation which contains the nucleon-nucleon (NN) strong and Coulomb interactions, we arrive at an equation for the intercluster relative motion functions χ. For the 0^+ bound state these functions are expanded in terms of products of tempered Gaussian functions $\exp(-\gamma_i \rho^2)$ [8] with different ranges γ_i for each type of relative coordinate. The expansion coefficients are determined from a variational principle. The scattering states are calculated from a Kohn-Hulthén variational method [8] for the S-matrix, which uses square integrable basis functions matched with the correct scattering asymptotics. Then, using the resulting eight-nucleon wave functions, the cross section (3) is evaluated.

The model used herein is essentially the same as that used in Refs. [9,10], which was used to describe the ^{7}Li, ^{7}Be, ^{8}Li, and ^{8}B nuclei, and the ^{7}Be$(p,\gamma)^8$B reaction. We use the same parameters for the description of ^{7}Li and ^{7}Be, and the same NN interaction (Minnesota force) as in Ref. [9]. Using these parameters, the ^{7}Li and ^{7}Be properties are well reproduced [9]. The calculated relative binding energies ^{7}Li(g.s.)–^{7}Be(g.s.) and ^{7}Li(g.s.)–^{8}Be(g.s.) are also close to the experimental values. Note that in eq. (3) the experimental value for E_γ is used.

We calculate the $E1$, $E2$, and $M1$ cross sections for the capture to the ground state of ^{8}Be. An unambiguous treatment of the transition to the broad 2^+ excited state of ^{8}Be would require a more sophisticated model.

We generate the 0^+ bound state and 1^-, 2^+, and 1^+ scattering states using the same force in all cases. In order to account for specific distortions of ^{7}Li and ^{7}Be, we describe these nuclei by using six basis states.

The result of the calculation of the ^{7}Li$(p,\gamma)^8$Be cross section is presented in Fig. 1 in terms of the astrophysical S factor

$$S(E) = \sigma(E) E \exp\left[2\pi\eta(E)\right], \tag{4}$$

where η is the Sommerfeld parameter. As our $E2$ cross section is 2–3 orders of magnitude smaller than the $E1$, it is not displayed. There is no contribution to the cross section coming from the second 1^+ state, as expected. The nonresonant part of the cross section and the first 1^+ state are well reproduced, although some $M1$ strength is missing in the resonance region.

In our model the 386 keV ($T = 1$) resonance is dominated by the $I = 1$ channel spin. This is in contradiction to experiment [11], which gives 3–5 for the ratio of the $I = 2$ to $I = 1$ channel spin contributions to the cross section. The same $I = 1$ dominance was also observed in the calculations of the 1^+ isobaric analogue state in ^{8}Li and ^{8}B. In order to understand the origin of this $I = 1$ dominance, we calculated the percentages of the orthogonal (LS) components in ^{8}Li (which is the only two-body bound state in the triplet). The $(LS) = (1,0)$, $(0,1)$, $(1,1)$, and $(2,1)$ components have 83.4%, 0.03%, 13.3%, and

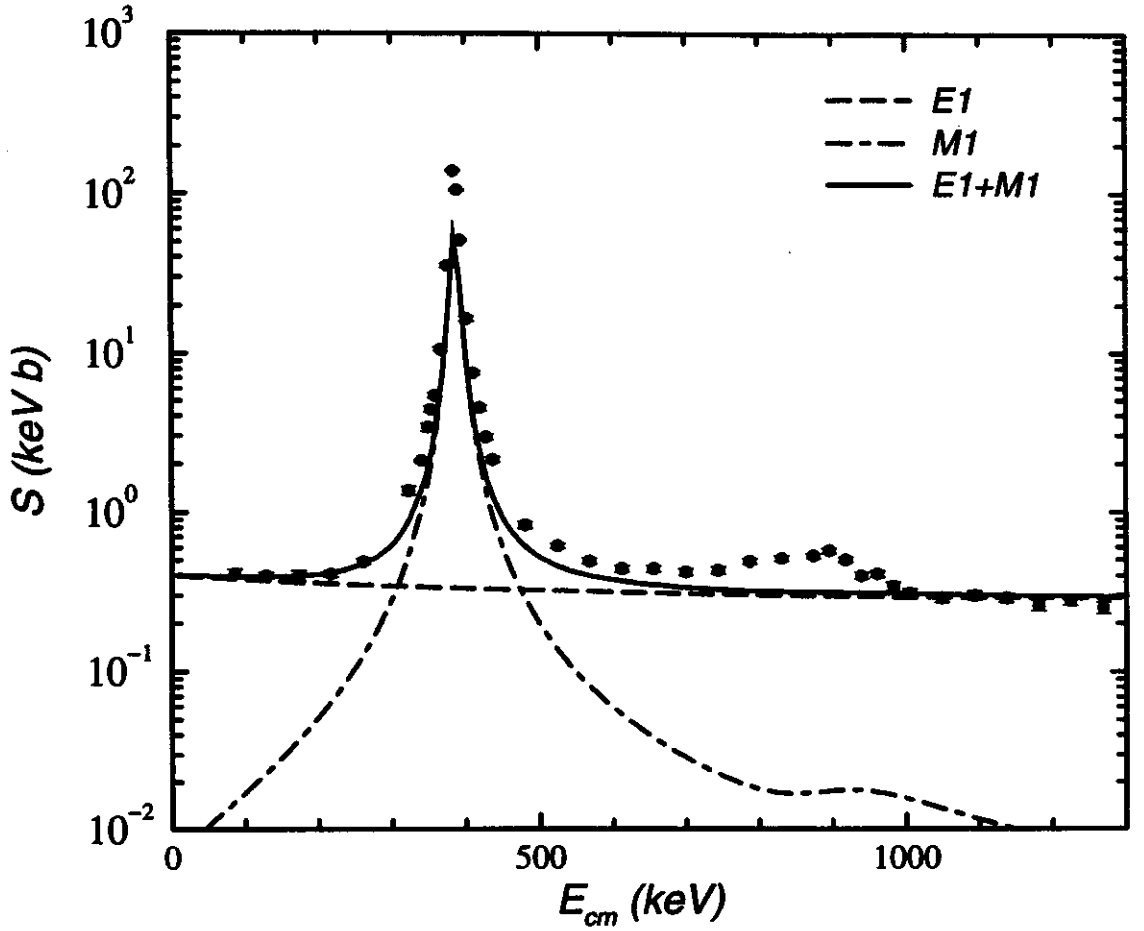

Figure 1: ^{7}Li$(p,\gamma_0)^8$Be astrophysical S factor as a function of the ^{7}Li+p center-of-mass energy. The result of the present calculation is given by the solid line, while the $E1$ and $M1$ contributions are given by the dashed and dot-dashed lines, respectively. The data are those of Zahnow *et al.* [3].

3.2% weights, respectively. However, the contribution of the largest component, $(1,0)$, to the $I=2$ channel spin state is zero, and hence the $I=1$ configuration dominates. Very similar (L,S) components were found in a different three-body model [12] using completely different cluster-cluster interactions. That model would also predict a dominant $I=1$ component in the $A=8$ $1^+;1$ triplet. In the second 1^+ $(T=0)$ state, our model predicts a dominant $I=2$ component. It remains a question as to whether the mixing of these states could influence the experimental determination of the channel spin ratio.

As a comparison to the results obtained from our RGM model, the $I=1,2$ spectroscopic amplitudes were calculated using wave functions obtained from a large space shell model calculation. The interaction used was that of Zheng *et al.* [13], based on a multi-valued G-matrix calculation and defined within the complete $(0+2+4)\hbar\omega$ shell model space. The calculations were performed using the shell model code OXBASH [14]. The spectroscopic amplitudes $S_{I=1,2}$ are defined in terms of the shell model spectroscopic amplitudes by

$$S_I = \sum_j \alpha_{I,j}\theta_j, \tag{5}$$

where θ_j are the shell model spectroscopic amplitudes ($j = 3/2$ or 1/2),

$$\theta_j = \frac{1}{\sqrt{2J_f+1}} \left\langle J_f(^8\mathrm{Be}) \left\| a_j^\dagger \right\| I_7(^7\mathrm{Li}) \right\rangle, \tag{6}$$

and $\alpha_{I,j}$ are transformation coefficients for the recoupling of the angular momenta in terms of the channel spin, I,

$$[I_7, j]\, J_f \rightarrow \left[\left(J_i, \frac{1}{2} \right) I, l_2 \right] J_f. \tag{7}$$

Table 1 lists the spectroscopic amplitudes, S_I, as obtained from our shell model calculation, along with

Table 1: Spectroscopic amplitudes, S_I, labeled by the channel spin I for the $^7\mathrm{Li}(p,\gamma)^8\mathrm{Be}$ reaction to the 1^+ states in ^{8}Be, as obtained from the shell model calculations using the interactions of Zheng *et al.* [13] and of Cohen and Kurath [15].

			S_I	
State	$E_{c.m.}$ (keV)	I	Zheng	CK
$1^+;1$	386	1	0.3499	0.2644
		2	0.2774	0.3910
$1^+;0$	897	1	−0.2612	−0.2773
		2	0.5132	0.5623

those obtained from the calculation using the Cohen and Kurath (CK) $(6-16)$2BME $0p$-shell interaction [15]. Note that the contribution from higher shells to the amplitudes calculated in the $(0+2+4)\hbar\omega$ space is negligible. The CK amplitudes favor the $I = 2$ channel spin for the $1^+;1$ state, while the Zheng ones support the results of our analysis. This discrepancy is the result of a slight redistribution of particle strength between the $0p_{3/2}$ and $0p_{1/2}$ orbits, as is illustrated in Table 2. The spectroscopic amplitude, θ_j,

Table 2: Spectroscopic amplitudes, θ_j, for the $^7\mathrm{Li}(p,\gamma)^8\mathrm{Be}$ reaction to the 1^+ states in ^{8}Be, as obtained from our shell model calculations.

			θ_j	
State	$E_{c.m.}$ (keV)	j	Zheng	CK
$1^+;1$	386	$0p_{3/2}$	0.4327	0.4009
		$0p_{1/2}$	−0.1104	−0.2490
$1^+;0$	897	$0p_{3/2}$	−0.0290	−0.0334
		$0p_{1/2}$	−0.5752	−0.6266

for the capture to the $0p_{3/2}$ orbit is larger in the Zheng model, while there is a corresponding decrease in the magnitude for the capture to the $0p_{1/2}$ orbit.

We note that if our cluster model does in fact give the incorrect channel spin ratio, then the singlet-odd component of the NN force is probably responsible. In our model we calculate the peak to 80 keV S factor ratio for the $I = 1$ and $I = 2$ channel spin contributions. Using these numbers we can estimate the $M1$ strength at 80 keV for any given channel spin ratio.

The contribution of the $M1$ component to the total S factor at 80 keV is 3.5%. If one adopts a value of 3.2 for the $I = 2/I = 1$ channel spin ratio, together with the experimental width and peak value of the 386 keV resonance, this $M1$ contribution is 6.3%, consistent with the estimates by Barker [5]. The value of 20% determined from the analysis of Chasteler *et al.* [1] may be due to the assumption of a negligible $0p_{3/2}$ spectroscopic factor. That assumption is not supported by the results of the shell model calculations presented in Table 2.

a. Present address: Theoretical Division, Los Alamos National Laboratory, Los Alamos, New Mexico, 87545

References

1. R. M. Chasteler, H. R. Weller, D. R. Tilley, and R. M. Prior, Phys. Rev. Lett. 72 (1994) 3949.
2. C. Rolfs and R. W. Kavanagh, Z. Phys. A 350 (1994) 93.
3. D. Zahnow, C. Angulo, C. Rolfs, S. Schmidt, W. H. Schulte, and E. Somorjai, Z. Phys. A 351 (1995) 229.
4. H. R. Weller and R. M. Chasteler, Z. Phys. A 352 (1995) 353.
5. F. C. Barker, Aust. J. Phys. 48 (1995) 813.
6. M. A. Godwin, R. M. Chasteler, C. M. Laymon, R. M. Prior, D. R. Tilley, and H. R. Weller, Phys. Rev. C 53 (1996) R1.
7. P. Descouvemont and D. Baye, Nucl. Phys. A 407 (1983) 77; *ibid.* 487 (1988) 420; *ibid.* 573 (1994) 28; T. Mertelmeier and H. M. Hofmann, Nucl Phys. A 459 (1986) 387.
8. M. Kamimura, Prog. Theor. Phys. Suppl. 68 (1980) 236.
9. A. Csótó, Phys. Lett. B 315 (1993) 24.
10. A. Csótó, K. Langanke, S. E. Koonin, and T. D. Shoppa, Phys. Rev. C 52 (1995) 1130.
11. Ma60 B. Mainsbridge, Nucl. Phys. 21 (1960) 1.
12. Shulgina N. B. Shul'gina, B. V. Danilin, V. D. Efros, J. M. Bang, J. S. Vaagen, and M. V. Zhukov, Nucl. Phys. A 597 (1996) 197.
13. D. C. Zheng, B. R. Barrett, J. P. Vary, W. C. Haxton, and C.-L. Song, Phys. Rev. C 52 (1995) 2488.
14. OXBASH-MSU (the Oxford-Buenos-Aries-Michigan State University shell model code). A. Etchegoyen, W. D. M. Rae, and N. S. Godwin (MSU version by B. A. Brown, 1986); B. A. Brown, A. Etchegoyen, and W. D. M. Rae, MSUCL Report Number 524 (1986) (unpublished).
15. S. Cohen and D. Kurath, Nucl. Phys. 73 (1965) 1.

PARITY VIOLATION IN THE $17/2^-$ ISOMER OF ^{93}Tc

B.A. Brown

Parity nonconservation originates at the most fundamental level from the weak currents mediated by the exchange of the W and Z bosons. PNC in nuclei was the first place where the nonstrangeness-changing sector of the standard weak-interaction model was observed [2]. Nuclear PNC is usually interpreted in terms of the underlying nucleon-nucleon (NN) PNC. Theoretical values for the nominal "best value" strengths of NN PNC interactions were established by Desplanques, Donoghue and and Holstein (DDH) [3] and their hadronic model dependence has been investigated [3,4].

In order to experimentally establish the strengths of the isoscalar (IS), isovector (IV) and isotensor (IT) components of the NN PNC interaction, it is important to compare results from NN scattering with those from nuclear bound states. The interpretation of the results for the nuclear bound states depends upon accurate nuclear-structure calculations. For a few nuclei, such as ^{18}F and ^{19}F, much of the nuclear-structure uncertainty can be removed by comparison to the analogue axial-charge beta decays [2], and in general for light nuclei large-scale shell-model calculations can be carried out [2,5]. The upper limit for the empirical strength of the IV component found from light nuclei [5] is a factor of three smaller than the DDH "best value" based upon the SU(3) quark model plus penguin-diagram corrections. This is surprising because it is this component which was predicted to be enhanced by the neutral current, Z-boson, contribution which is unique to the nonstrangeness changing PNC [3]; never-the-less, is it still within the range allowed by hadronic models [3].

There are many cases, such as in ^{180}Hf [6], where nuclear PNC has been observed, but where the interpretation is limited by the uncertainties in the nuclear wave functions [2]. Recently, large PNC effects in low-energy neutron scattering have been observed, and the interpretation of the results for these compound nucleus states has focused on the nuclear many-body "enhancement" factor [7]. All bound-state cases studied to date are thought to be dominated by the "one-body" nuclear mechanism which originates from a coherent average of the NN PNC interaction over all core nucleons and which yields single-particle matrix elements $< l, j|V_{PNC}|l-1, j >$ on the order of one eV

The case of ^{93}Tc presents a unique situation. The structure of the nuclei with 50 neutrons near ^{93}Tc are well described by shell-model wave functions [8,9], and thus reasonable nuclear-structure calculations can be carried. It is different from the cases studied in light nuclei because it is a high-spin doublet and because there is (in the simplest model) no "one-body" component – it is entirely two-body. In particular, we will show below that the ^{93}Tc PNC is particularly sensitive to the isotensor component of the NN PNC potential.

The $\frac{17}{2}^-$ isomeric level of ^{93}Tc has a $\frac{17}{2}^+$ partner at a separation of only 300 eV [10,11]. The isomer decays to a $\frac{13}{2}^+$ state through a mixed M2/E3 transition. Any contribution of the opposite parity $\frac{17}{2}^+$ state would lead to an E2 admixture to the transition whose intrinsic transition matrix element is larger by a factor of $\sim$ 1000 than M2 and E3. For a polarized sample of the isomer, the mixed parity component in the transition introduces a $P_1(\cos\theta)$ term in the angular distribution with respect to the direction of polarization, yielding a 0° - 180° asymmetry A_γ of the decay γ-rays. This small asymmetry has recently

TABLE I. PNC matrix elements (in units of meV)

term		Model A	Model B	Model C	Model D
IS_1	$-g_\rho h_\rho^{(0)}(1+\chi_v)$	3.05	2.39	0.17	
IS_2	$-g_\rho h_\rho^{(0)}$	0.40	0.35	0.42	
IS_3	$-g_\omega h_\omega^{(0)}(1+\chi_s)$	0.28	0.22	0.20	
IS_4	$-g_\omega h_\omega^{(0)}$	0.20	0.18	0.01	
Σ IS_i		3.93	3.14	0.80	0.01
IV_1	$f_\pi g_{\pi NN}$	0	0	−4.36	
IV_2	$-g_\rho h_\rho^{(1)} - g_\omega h_\omega^{(1)}$	0.13	0.11	0.07	
IV_3	$-g_\rho h_\rho^{(1)}(1+\chi_v) - g_\omega h_\omega^{(1)}(1+\chi_s)$	0.22	0.17	0.15	
IV_4	$g_\rho h_\rho^{(1)} - g_\omega h_\omega^{(1)}$	0	0	−0.06	
IV_5	$-g_\rho h_\rho^{\prime 1}$	0	0	−0.07	
Σ IV_i		0.35	0.28	−4.26	−4.33
IT_1	$-g_\rho h_\rho^{(2)}$	0.13	0.12	0.14	
IT_2	$-g_\rho h_\rho^{(2)}(1+\chi_v)$	1.05	0.82	1.10	
Σ IT_i		1.18	0.94	1.26	1.02
Σ		5.46	4.36	−2.20	−3.30

been measured by Hass et al.[12] and has been used to deduce a parity nonconserving matrix element of

$$|(\frac{17^-}{2}|H_{pnc}|\frac{17^+}{2})| = 0.59(19)(25)meV \ ,$$

where the errors shown are the statistical error and the error associated with the nuclear physics parameters and polarization of the intial state.

In contrast to ^{180}Hf, the ^{93}Tc isomer has a more transparent structure of 5 valence protons outside the ^{88}Sr core. We have carried out calculations based upon the "best-value" PNC interaction of Desplanques, Donoghue and and Holstein (DDH) [3]. The results in Table I are broken down into four isoscalar (IS), five isovector (IV) and two isotensor (IT) components each of which is labeled by the particular meson-nuclear coupling constant to which it is proportional. The method of calculation including the description of the short-range correlations is the same as used in Refs. [5] and [13]. Harmonic-oscillator radial wave functions with $\hbar\omega$=8.7 MeV are used. PNC matrix elements between single-particle states which have the same j value but different ℓ values pick up a coherent (one-body) contribution from all occupied orbitals and tend to be the terms which dominate PNC observables in light and heavy nuclei. The case of ^{93}Tc is unique special in this regard because this one-body contribution is not allowed by the dominant $1p_{1/2}$ and $0g_{9/2}$ valence wave functions.

Model A is the simple $1p_{1/2} - 0g_{9/2}$ model space used by Morrison and McKellar [14]. We used the "seniority-conserving" interaction of Glockner and Serduke [8]. The Morrison-McKellar calculations use the PNC interaction of Desplanques and Missimer (DM) which is somewhat older than DDH. But the DM and DDH PNC interactions are similar and the results given in Table I (with a total 5.5 meV) are close to those obtained by Morrison and McKellar – both are nearly an order of magnitude larger than the present experiment. We note that the IV terms are small in Model A since the dominant pion-exchange contribution (IV_1) has an isospin structure which vanishes for T=1 two-body configurations. The PNC observables in light nuclei are consistent with an IS contribution which is 0.5 to 1.2 times the DDH best-value [5]. If we were to take the lower value of 0.5, the total PNC matrix element of 3.5 meV is still much larger than experiment. The isotensor contribution (IT) is usually small compared to the IS and IV terms since it does not contribute the the one-body PNC matrix element. In addition, the IT contribution does not contribute to ^{18}F and ^{19}F because of isospin selection rules and in the case if ^{14}N it turns out to be small [15]. The case of ^{93}Tc is thus the first which we are aware of where the experimental PNC matrix element is comparable to the size of the expected IT contribution.

We now consider Model B where the model space is enlarged to include $0f_{5/2}$, $1p_{3/2}$, $1p_{1/2}$ and $0g_{9/2}$. We have calculated the PNC matrix elements in the full Model B space with the strong interaction of Ji and Wildenthal [9]. The results for the ^{93}Tc PNC matrix element given in Table I are not very different from the Model A results and are still much larger than experiment.

Now we examine the effects beyond the space of Model B. The most important excitations to consider are: (a) $1s_{1/2} \rightarrow 1p_{1/2}$, (b) $1p_{1/2} \rightarrow 2s_{1/2}$ and (c) $0g_{9/2} \rightarrow 0h_{9/2}$. These are important because even though the amplitude may be small, in each case the PNC matrix element picks up a coherent contribution from all of the core nucleons. Consider, for example, process (b) in terms of the zeroth-order two-body matrix element $<0g_{9/2}^2, 4^+ \mid H_{pnc} \mid 0g_{9/2}, 1p_{1/2}, 4^- >$ (which has a DDH value of 22 eV) as shown diagrammatically in fig. 5a. The first-order correction diagrams corresponding to the $2s_{1/2}$ admixtures are shown in figs. (5b) and (5c). The strong interaction matrix element calculated with the interaction used in [16] is 0.12 MeV and the energy denominator is about 9 MeV. Diagram (5b) can be neglected since the

PNC matrix element is again just two-body (on the order of 10 meV). But diagram (5c) which represents a coherent sum over the core nucleons yields a PNC matrix element of the order of one eV and thus enters at the same level, (0.12 MeV)x(1 eV)/(9 MeV) = 13 meV, as the zeroth order two-body term (fig. 5a). The only terms of the form of diagram (fig. 5c) arise from the three contributions (a), (b) and (c) listed above.

We have made an explicit calculation of contribution (b) by enlarging the Model A to include the $2s_{1/2}$ orbital and then allowing one nucleon to be excited into this orbital (Model C). Following again the formalism of Refs. [13] and [5], all of the terms discussed above including the summation over the core nucleons are explicitly taken into account. The model space and interaction are described in [16]. In Table I we give the results obtained from this calculation. We indeed find a large change in the two PNC matrix elements, IS_1 and IV_1, which contribute to the coherent core summation. The additional contribution to IS_1 cancels with the zeroth order two-body term. The change in IV_1 brings in a new IV contribution. The other PNC operators, in particular the isotensor operator, do not contribute to the core summation and thus are not much effected by the $2s_{1/2}$ admixtures. We are not able to calculate the effects of contributions (a) and (c), however, they should be less important. Contribution (a) should be smaller than (b) because the $1p_{1/2}$ is most filled and the $1s_{1/2} \rightarrow 1p_{1/2}$ excitations are thus blocked. Contribution (c) should be smaller than (b) because the $0g_{9/2}$ proton orbital is not completely filled and because the $0g_{9/2} - 0h_{9/2}$ energy denominator is larger due to the spin-orbit splitting.

Model B and Model C are two independent enlargements of the simplest Model A. Since the enlargements are both relatively small in amplitude, in the spirit of perturbation theory, we should add the changes obtained from both together. Thus we arrive at the final results labeled Model D in Table I which are obtained by $M_D = M_A + [M_B - M_A] + [M_C - M_A]$, where M are the PNC matrix elements.

The total Model D value of (IS+IV+IT)=$(0.0 - 4.3 + 1.0) = -3.3$ meV changes sign from Model A but is still larger in magnitude than experiment. However, as mentioned in the introduction, in light nuclei it has been found that the IV term is experimentally strongly suppressed from the DDH value. If we were to reduce the IV contribution by the empirical factor of 0.15±0.15 found for light nuclei [5], then the total value would be [IS+IV+IT]=$[0.0 - (0.6 \pm 0.6) + 1.0] = -0.2$ to 1.0 meV in agreement with experiment. It appears that the PNC matrix element may be dominated by the isotensor term, but the theoretical uncertainties in the IS term must be considered more carefully. In particular, second-order effects, such as the excitation of two neutrons across the N=50 closed shell, should be examined.

In summary, we find that the PNC calculation for ^{93}Tc leads to rather complicated but potentially interesting conclusions when compared with the small experimental value. The PNC matrix element obtained in the simplest $1p_{1/2} - 0g_{9/2}$ model space is in itself very stable and much larger than the experimental value. Small admixtures of other orbitals strongly change the result for the IS and IV contributions. The isotensor contribution can be reliably calculated and, compared to other PNC observables, gives a large contribution compared with the experimental value. Agreement with experiment is improved if the IV DDH strength is reduced as observed for light nuclei.

References

1. Permanent address: Department of Particle Physics, Weizmann Institute of Science, Rehovot, Israel.
2. E. G. Adelberger and W. C. Haxton, Annu. Rev. Nucl. Part. Sci. 35, 501 (1985).
3. B. Desplanques, J. F. Donoghue and B. R. Holstein, Ann. Phys. (N.Y.) 124, 449 (1980).
4. G. B. Feldman, G. A. Crawford, J. Dubach and B. R. Holstein, Phys. Rev. C43, 863 (1991).
5. M. Horoi and B. A. Brown, Phys. Rev. Lett. 74, 231 (1995).
6. K.S. Krane, C.E. Olsen, James R. Sites and W.A. Steyert, Phys. Rev. C4, 1906 (1971).

7. J. D. Bowman, G. T. Garvey, M. B. Johnson and G. E. Mitchell, Annu. Rev. Nucl. Part. Sci. 43, 829 (1993).
8. D. H. Glockner and F. J. P. Serduke, Nucl. Phys. A220, 447 (1974).
9. X. Ji and B. H. Wildenthal, Phys. Rev. C37, 1256 (1988); Phys. Rev. C38, 2849 (1988).
10. B. A. Brown, D. B. Fossan, P. M. S. Lesser and A. R. Poletti, Phys. Rev. C13, 1194 (1976); B. A. Brown, R. A. Warner, L. E. Young and F. M. Bernthal, Phys. Rev. C17, 2040 (1978).
11. B.A. Brown, O.Häusser, T. Faesterman, D.Ward, H.R. Andrews and D.Horn, Nucl.Phys. A306, 242 (1978).
12. M. Hass et al., Phys. Lett. B, to be published.
13. B. A. Brown, W. A. Richter and N. S. Godwin, Phys. Rev. Lett. 45, 1681 (1980).
14. I. Morrison and B. H. McKellar, J. Phys. G6, L109 (1980).
15. E. G. Adelberger, P. Hoodbhoy and B. A. Brown, Phys. Rev. C30, 456 (1984); M. Horoi, G. Clausnitzer, B. A. Brown and E. K. Warburton, Phys. Rev. C50, 775 (1994).
16. B. A. Brown and K. Rykaczewski, Phys. Rev. C50, R2270 (1994).
17. H. A. Roth et al., Phys. Rev. C50, 1330 (1994).

GLOBAL BEHAVIOR OF OCTUPOLE VIBRATIONS IN NUCLEI

Vladimir Zelevinsky

The systematics of octupole vibrations was analyzed [1] over a wide range of Z and A using summed $B(E3)\uparrow$ values for all 3^- states in a given nuclide. Data obtained with the (p,p'), (d,d'), and (α,α') reactions were used, as opposed to an earlier study based on Coulomb excitation and lifetime data. Results of the new analysis support earlier observations of significant anharmonicity although the empirical situation is more complicated than in the quadrupole case analyzed earlier [2].

Collective models based on near-harmonic vibrations give for the reduced transition probability to the single-phonon excitation

$$B(E\lambda)\uparrow \equiv B(E\lambda; 0 \to \lambda) = \frac{2\lambda+1}{2D_\lambda \omega_\lambda} Q_\lambda^2. \tag{1}$$

Here Q_λ is the collective multipole moment, ω_λ is the phonon frequency and D_λ is the inertial parameter. The inverse dependence on the transition energy is a characteristic feature of any model with harmonic vibrations and "natural" transition operators. In the hydrodynamical model (small-amplitude shape vibrations of an incompressible liquid drop), the collective multipole moment is $Q_\lambda = (3/4\pi)ZeR^\lambda$ where Z is the nuclear charge and R is the average nuclear radius ($\propto A^{1/3}$). If the liquid motion is irrotational, the hydrodynamical mass parameter is, for mass number A, $D_\lambda^{irr} = (3/4\pi\lambda)mAR^2$ where m is the nucleon mass. Then the global behavior of transition probabilities is predicted as

$$B(E\lambda)\uparrow \propto Z^2 A^{(2\lambda-5)/3} \omega_\lambda^{-1} \rightsquigarrow B(E3)\uparrow \propto \frac{Z^2R^6}{D_3}\frac{1}{E_{3^-}} \propto Z^2 A^{\frac{1}{3}} (E_{3^-})^{-1}. \tag{2}$$

Therefore, the natural fit for the data is

$$B(E3)\uparrow Z^{-2}A^{-\frac{1}{3}} = K E_{3^-}^{\eta}, \tag{3}$$

where K and η are the fit parameters. The results [1] (typically, η between -0.75 and -0.9) show that octupole transitions are generally not harmonic, but that subsets of nuclei, particularly near Pb, may undergo harmonic octupole vibrations. The overall systematics [2] for quadrupole transitions, $\lambda = 2$, confirms the ω_2^{-1} dependence, but clearly prefers $\sim A^{-2/3}$ scaling, whereas eq.(2) gives $\sim A^{-1/3}$ (and $\sim A^{1/3}$ in the octupole case).

The residual interactions and shell effects make non-magic nuclei much softer than in the hydrodynamical model. In the microscopic approach, low-lying collective vibrations appear as coherent sound-like two-quasiparticle excitations rather than surface hydrodynamical waves. Pairing is essential in this description because the frequencies as a rule fall within the pairing gap $2\bar{E}$.

For the quadrupole case, non-magic spherical nuclei are at the limit of the phase transition to static deformation. Therefore we can make estimates of $B(E\lambda)\uparrow$ near the critical point where the restoring force vanishes [3]. Strong anharmonic effects, mostly due to the quartic anharmonicity [4], stabilize the

nucleus. One comes to the simple expression for the global behavior of the transition probabilities:

$$B(E\lambda)\uparrow = \frac{2\lambda+1}{2}e^2\left(\frac{Z}{A}\right)^2 \Omega q_\lambda^2 \frac{2\bar{E}}{\omega_\lambda}. \tag{4}$$

Here, $q_\lambda \simeq \langle r^{2\lambda}\rangle \xi^2$ is the typical reduced matrix element for a single-particle transition ($\xi \simeq 1/2$ is an average reduction factor connected with the pairing effects), and $2\bar{E} \simeq \epsilon_F/\sqrt{A}$ is the two-quasiparticle excitation energy. The factor $\Omega \simeq \sqrt{A}$ characterizes the degree of collectivity of the phonon mode. In the quadrupole case, using $\langle r^4\rangle = 0.95A^{4/3}\mathrm{fm}^4$, we obtain ($\omega_2$ is given in keV)

$$B(E2)\uparrow \simeq 8.5\xi^2 Z^2 A^{-2/3}\omega_2^{-1}e^2\mathrm{b}^2. \tag{5}$$

We can directly compare this with the empirical fit of Raman *et al.* [2],

$$B(E2)\uparrow = (2.6\pm 0.6)Z^2A^{-2/3}\omega_2^{-1}e^2\mathrm{b}^2. \tag{6}$$

Although the numerical agreement may be coincidental, the general trend is reproduced in a natural way. Because the zero-point vibrational amplitude in soft spherical nuclei is of the same order of magnitude as the static quadrupole deformation in permanently deformed nuclei, we expect the same estimate to be valid for rotational excitations as well. This is confirmed in Ref. [2].

Low-lying octupole excitations appear less regularly and do not have energies as low as those of quadrupole modes. The reduced transition probabilities in the hydrodynamical model are predicted as

$$B(E3)\uparrow\ Z^{-2}A^{-1/3} \approx 2.2\times 10^{-4}[\omega_3(\mathrm{MeV})]^{-1}e^2\mathrm{b}^3. \tag{7}$$

The value of K thus obtained is larger than that seen in the fits by an order of magnitude. The inverse energy dependence shown here is stronger than that seen in the fits.

The microscopic model used in the quadrupole case gives a different A-dependence for the octupole mode. Expressed in a form similar to eq. (7), it reads

$$B(E3)\uparrow\ Z^{-2}A^{-1/3} \approx 15\times 10^{-5}(\Omega A^{-5/6})\xi^2[\omega_3(\mathrm{MeV})]^{-1}e^2\mathrm{b}^3. \tag{8}$$

The collectivity factor Ω should be weaker here than in the quadrupole case ($\sim A^{1/2}$). Because the elementary octupole excitation involves an intruder single-particle level, we expect $\Omega \sim A^{1/3}$. Then the numerical coefficient in (8) becomes $15\times 10^{-5}A^{-1/2}\xi^2 \simeq 0.4\times 10^{-5}$ for medium mass nuclei, which is too small when compared to the fitted value of $K \approx (1.5-2.3)\times 10^{-5}$. The nonadiabatic corrections bring the estimate closer to the average K seen in the fits. However, they do not explain the trend of the effective exponent η towards the values $\eta < 1$.

Intrinsic anharmonicity of the octupole mode should be weak, because the negative parity does not permit mixing of one- and two-phonon states. However, the interaction of octupole excitations with the soft quadrupole mode can be quite important. This leads to the phenomenological hamiltonian

$$H = H_2 + H_3^{(0)} + x\sum_\mu [(f^\dagger f)_{2\bar{\mu}}d_\mu + d_\mu^\dagger (f^\dagger f)_{2\mu}] \tag{9}$$

where H_2 stands for the quadrupole part, including all anharmonic corrections, and $H_3^{(0)}$ is the purely harmonic octupole vibrator $H_3^{(0)} = \sum_\mu \omega_3 f_\mu^\dagger f_\mu$; f_μ and d_μ are the octupole and quadrupole boson operators,

respectively. This hamiltonian gives for the energy E_3 of the lowest octupole excitations

$$E_3 = \omega_3 - a\frac{x^2}{\omega_2} \tag{10}$$

where the numerical factor a can depend on the details of the quadrupole anharmonicity. The coupling constant x in the model Hamiltonian can be calculated microscopically in the same way as quadrupole anharmonic terms [5]; it depends smoothly on the octupole frequency ω_3. Then the main modification of the global expression (8) would be the substitution of ω_3, which was identified in the harmonic approximation with the excitation energy E_3, by $E_3 + (\text{const})/\omega_2$. If this is the case, we may expect an anticorrelation of the transition probability $B(E3)$ with the quadrupole frequency ω_2.

In addition, the octupole vibrations are more surface-like than quadrupole ones. In the limit of surface waves on a liquid drop, the normal frequencies are scaled as $\omega \propto A^{-1/2}$. If the collective strength can grow as $\Omega \propto (\text{area}) \propto A^{2/3}$, then we have from eq. (8), $B(E3) \propto \omega^{-2/3}$. In this limiting case, $\eta = -2/3$, and the actual situation lies in the range $-1 < \eta < -2/3$. Either or both of these effects can lead to deviations of η from the harmonic value, in particular placing it in the range seen in the fits.

These results are particularly relevant because a new generation of radiocative ion beam facilities will make possible the measurement of $B(E3)$ values in many unstable isotopes via scattering reactions in inverse kinematics.

References

1. M. P. Metlay, J. L. Johnson, J. D. Canterbury, P. D. Cottle, C. W. Nestor, Jr., S. Raman and V. G. Zelevinsky. Phys. Rev. C (1995).
2. S. Raman, C. W. Nestor, Jr., S. Kahane, and K. H. Bhatt, Phys. Rev. C 43, 556 (1991).
3. V. G. Zelevinsky, Int. J. Mod. Phys. E2, 273 (1993).
4. O. K. Vorov and V.G. Zelevinsky, Nucl. Phys. A439, 207 (1985).
5. V. G. Zelevinsky, in *Proceedings of the International Conference on Perspectives for the Interacting Boson Model* (Padova, 1994), p. 307.

PAIRING PHASE TRANSITION IN INDIVIDUAL NUCLEAR WAVE FUNCTIONS

Vladimir Zelevinsky, B. Alex Brown and Mihai Horoi

Energy levels and stationary wave functions obtained in realistic shell-model calculations [1, 2, 3] show generic signatures of quantum chaos. The nearest level spacing distribution and spectral rigidity agree with the predictions for the Gaussian orthogonal ensemble. New features are displayed by the complexity of individual wave functions and its regular evolution along the spectrum [1] which can be translated into the language of thermalization and decoherence [2, 3].

The stochastization of nuclear dynamics is accompanied by the evolution of collective motion, in particular, pairing. The lowest states reveal strong pairing correlations rapidly decreasing with temperature similar to the phase transition in superconductors. The correlations are caused by the enhanced attractive matrix elements of the two-body interaction $\langle (j_2^2)_{J=0,T=1}|V|(j_1^2)_{J=0,T=1}\rangle$. Isovector pairing is appropriate for light nuclei with protons and neutrons on the same orbitals. In the shell model we have the exact eigenfunctions which contain all interaction effects including pairing with the conservation laws of particle number, total angular momentum J and total isospin T strictly fulfilled. Therefore we do not need any BCS-type approximations.

We select as a probe the operator

$$\mathcal{H}_P = (P^\dagger \cdot P) \equiv \sum_{t=0,\pm 1} P_t^\dagger P_t \tag{1}$$

where the isovector pair annihilation (P_t) and creation ($P_t^\dagger$) operators with the isospin projection t are defined in terms of fermion operators $a_\lambda \equiv a_{ljm\tau}$ and $a_\lambda^\dagger$ according to

$$P_t = \frac{1}{\sqrt{2}} \sum_{lj} [\tilde{a}_{lj}\tilde{a}_{lj}]_{J=0,T=1,T_3=t}, \quad P^\dagger = \frac{1}{\sqrt{2}} \sum_{lj} [a_{lj}^\dagger a_{lj}^\dagger]_{J=0,T=1,T_3=t}. \tag{2}$$

Here the sums are taken over all single-particle orbitals lj. We have calculated the expectation value of $\mathcal{H}_P$ for all individual $J^\pi T = 0^+0$ states in two systems, 8 valence particles in ^{24}Mg ($N = 325$ states) and 12 valence particles in ^{28}Si ($N = 839$). The qualitative picture is the same in both cases, Fig. 1. At low excitation energy the states have a considerably higher value of $\langle \mathcal{H}_P \rangle$. This value drops very fast into a long smoothly decreasing tail. The fluctuations of $\langle \mathcal{H}_P \rangle$ are small, so that one can consider (1) as a function of excitation energy or temperature.

The simple fit to the observable energy dependence is given by

$$\langle \mathcal{H}_P \rangle = \overline{\mathcal{H}} + \mathcal{H}_c(E) + \mathcal{H}_{fl}(E) \tag{3}$$

where $\mathcal{H}_c(E)$ represents the condensate contribution and $\mathcal{H}_{fl}(E)$ corresponds to the pairing fluctuations. These effects, in turn, can be described as

$$\mathcal{H}_c(E) = A \frac{1-(E/E_c)}{1-(E/E_0)} \theta(E_c - E), \tag{4}$$

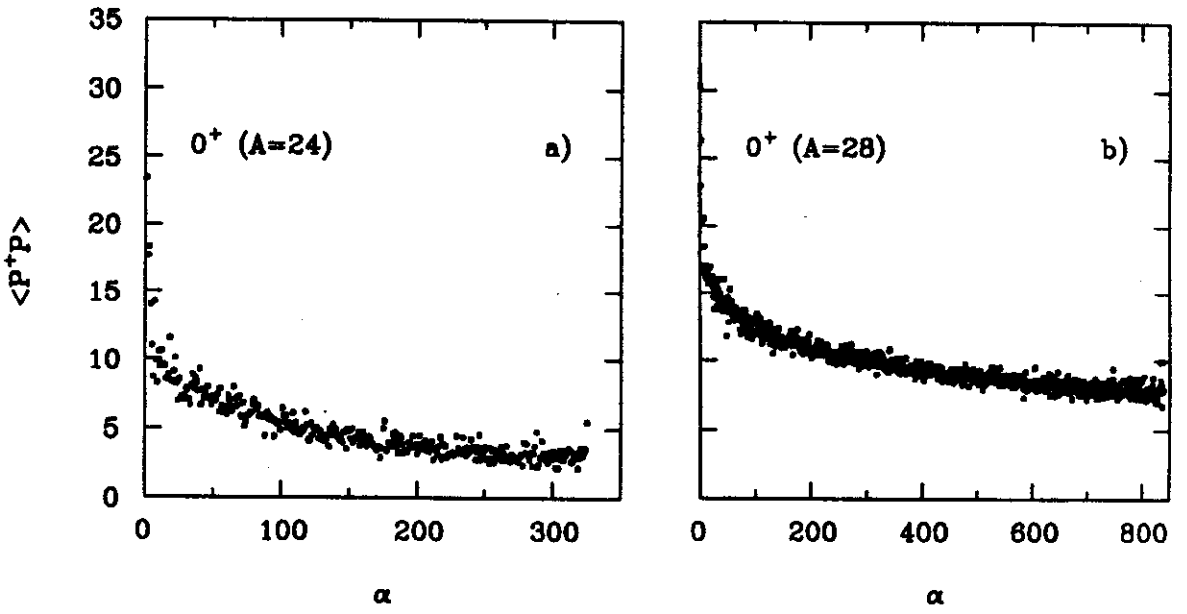

Figure 1: Expectation values $\langle \mathcal{H}_P \rangle$ of the operator (1) (dots) for all 0^+0 states $|\alpha\rangle$ of $A_v = 8$ articles (^{24}Mg), panel a, and $A_v = 12$ particles (^{28}Si), panel *b*.

$$\mathcal{H}_{fl}(E) = B \exp[-(E - E_c)/w]. \tag{5}$$

Here E_0 corresponds to the middle of the spectrum. The shell model level density can be described [1, 3] by the Gaussian with the centroid at E_0 and the width σ_E. This determines thermodynamic entropy and temperature $T = \sigma_E^2/(E - E_0)$. According to (4), the condensate disappears at the transition point $E = E_c$, or, in the temperature scale, at $T = T_c$. For the order parameter $\Delta \propto \sqrt{\mathcal{H}_c}$ the parameterization (4) gives the behavior

$$\Delta = \Delta_0 \sqrt{1 - \frac{T}{T_c}} \tag{6}$$

typical for the second order phase transition in the mean field approximation. The constant term $\overline{\mathcal{H}}$ describes the background value which would exist even with no attractive interaction in a normal Fermi gas. The fit is shown as a function of temperature T in Fig. 2. A clear signature of the phase transition in a small system is seen through the properties of individual eigenfunctions. The interesting feature of the data is the presence of a long exponential tail of pairing fluctuations far beyond the transition point.

The average quantity (1) can be independently estimated in many ways. The maximum possible value (=54 for of 12 valence particles) corresponds to the isospin invariant generalization of the degenerate seniority model. However the real value is far from that being strongly determined by the single-particle energies in the mean field.

The average of the operator (1) over the whole Hilbert space (no restrictions by angular momentum or isospin) can be calculated with the prescriptions of statistical spectroscopy for A_v valence nucleons

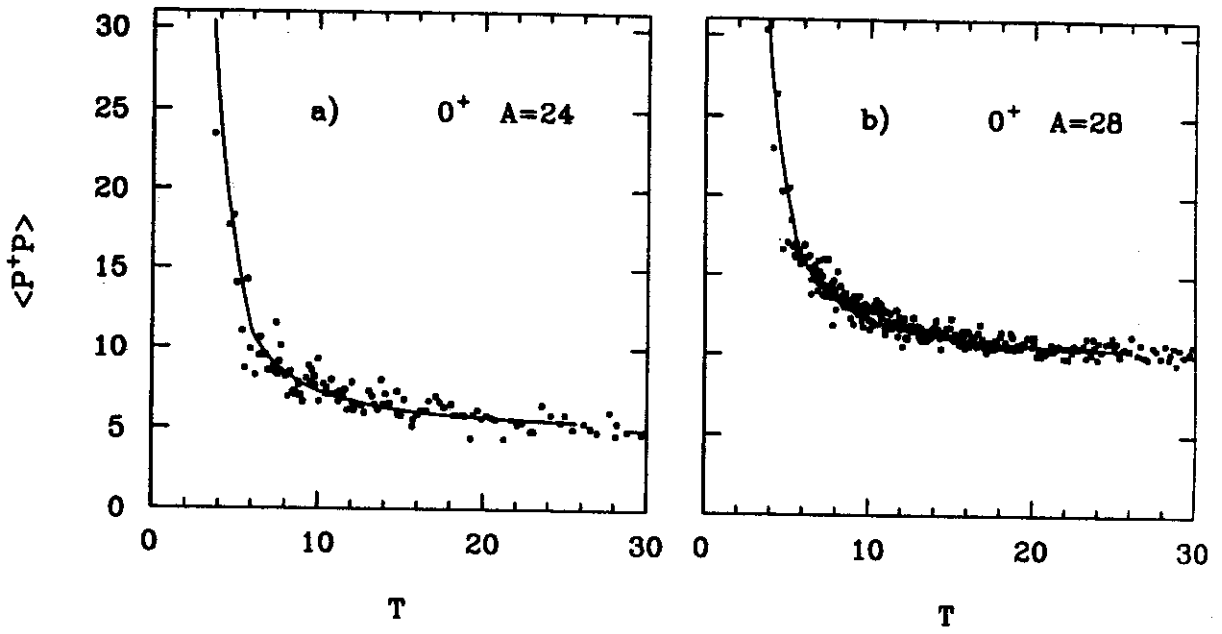

Figure 2: Expectation values $\langle \mathcal{H}_P \rangle$ of the operator (1) for individual 0^+0 states of ^{24}Mg, part a, and ^{28}Si, part *b*, dots, as a function of thermodynamic temperature. The solid lines correspond to the fit given by eqs. (3 - 5).

distributed over Ω (=12 for the *sd*-shell) spin-spatial orbitals,

$$\langle \mathcal{H}_P \rangle = \frac{3}{2(2\Omega - 1)} A_v (A_v - 1). \tag{7}$$

This estimate, $\langle \mathcal{H}_P \rangle = 8.6$ and 3.7 for $A_v = 12$ and 8 respectively, is to be compared to the behavior observed in our data. A close estimate can be obtained by taking the Fermi-gas average of the operator (1). Assuming the time reversal symmetry of the occupancies, $f_{\bar{\lambda}} = f_\lambda$, and their identity for neutrons and protons, we obtain

$$\langle \mathcal{H}_P \rangle = 3 \sum_{ljm} f_{ljm}^2. \tag{8}$$

Fig. 3, solid line, shows the relation between the tilted actual behavior of the pairing correlator and the nearly constant single-particle effect (8) calculated for the actual occupation numbers found in [2] for the 0^+0 states in ^{28}Si.

References

1. V.Zelevinsky, M.Horoi and B.A.Brown, Phys. Lett. B350, 141 (1995).
2. M.Horoi, V.Zelevinsky and B.A.Brown, Phys. Rev. Lett. 74, 5194 (1995).
3. V.Zelevinsky, B.A.Brown, N. Frazier and M.Horoi. Phys. Reports, *in press*.

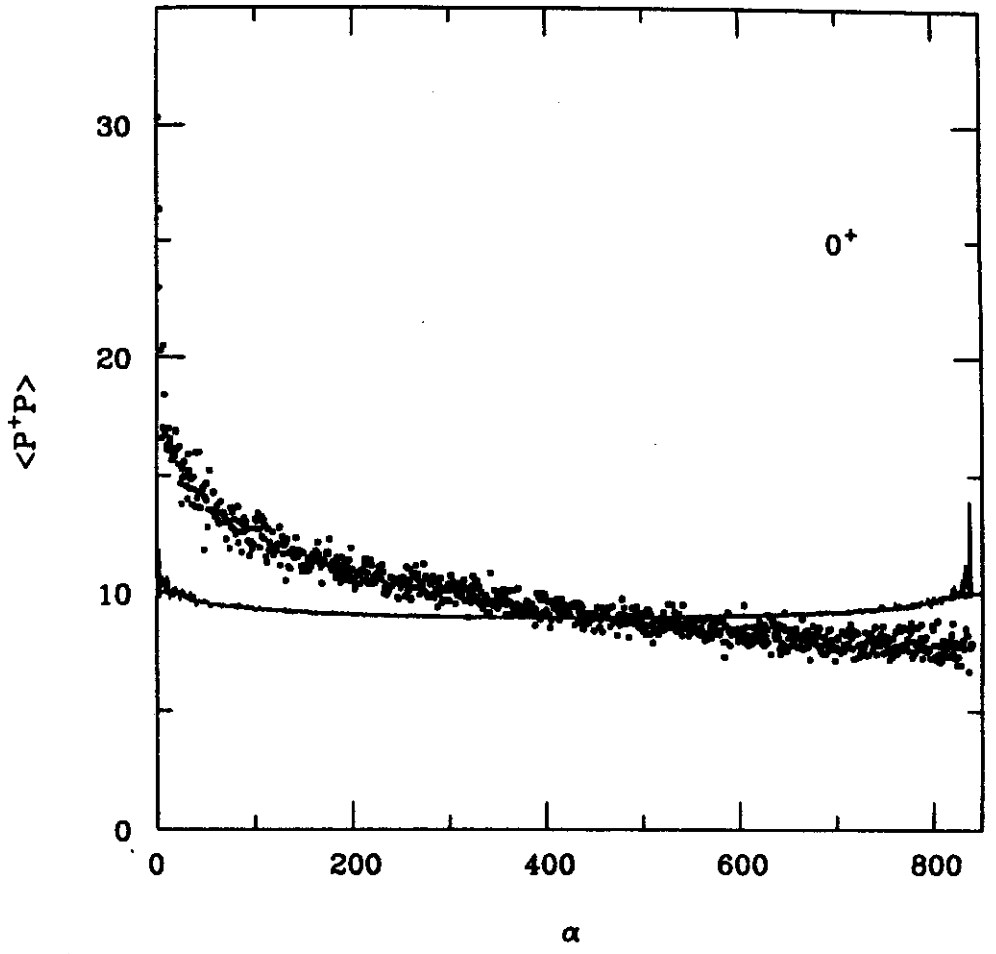

Figure 3: Comparison of the expectation values $\langle \mathcal{H}_P \rangle$ for the 0^+0 states of ^{28}Si (dots) and the Fermi-gas estimate (8) (solid line).

ASSESSMENT OF LARGE BASIS SHELL MODEL WAVE FUNCTIONS FOR THE Li ISOTOPES

S. Karataglidis, B. A. Brown, P. J. Dortmans[a], and K. Amos[a]

While the shell model is the most fundamental of nuclear structure models, states in light nuclei have been successfully described also in terms of clusters. The shell model should reflect such clustering, and that we seek to assess. The Li isotopes are good examples with which the shell model can be tested for cluster-like behavior, as large space (no core) shell model wave functions may be constructed [1], and the ^{6,7}Li ground states are known cluster–like states ($\alpha + d$ and $\alpha + t$, respectively). We have analyzed electron and proton scattering data using the same shell model wave functions seeking thereby to make a stringent test of those wave functions.

In principle, the strong clustering observed in the ground states of ^{6}Li and ^{7}Li should be contained in the wave functions obtained from the shell model. In each case, the inner $0s$-core may be assumed to be the α-cluster, with the valence $0p$-shell particles forming the other. In a simple $0\hbar\omega$ shell model picture, however, this does not take into account any interactions between these clusters and so higher–$\hbar\omega$ admixtures are needed in a realistic model. Thus we have considered shell model wave functions obtained from $0\hbar\omega$, $(0+2)\hbar\omega$, and $(0+2+4)\hbar\omega$ shell model spaces.

Various interactions were used in the shell model calculations to obtain the wave functions. They are: (a) the Cohen and Kurath $(6-16)$2BME interaction (CK) [2] for the $0\hbar\omega$ model space; (b) the MK3W interaction [3] for the complete $(0+2)\hbar\omega$ shell model space which encompassed all the shells from the $0s_{\frac{1}{2}}$ up to, and including, the $0f1p$-shells; and (c) the multi-valued g matrix interaction of Zheng *et al.* [1] for the $(0+2+4)\hbar\omega$ (Z4) space calculations. Also, the $0\hbar\omega$ (Z0) and $(0+2)\hbar\omega$ (Z2) g matrix interactions of Zheng [4] were considered to make comparisons with results obtained with the fitted (phenomenological) interactions.

In our first studies, we have considered the ground, $3^+;0$ (2.186 MeV), and $0^+;1$ (3.563 MeV) states in ^{6}Li, and the ground, $\frac{1}{2}^-;\frac{1}{2}$ (0.478 MeV) and $\frac{7}{2}^-;\frac{1}{2}$ (4.630 MeV) states in ^{7}Li; the energies of which are listed in the table as are the results of the various shell model calculations. The importance of increasing the size of the model space is illustrated for both nuclei. For example, the energies of the $\frac{1}{2}^-$ (0.478 MeV)

Table 1: The low-energy spectra of ^{6}Li and ^{7}Li as calculated in the $0\hbar\omega$ (CK and Zheng interactions), $(0+2)\hbar\omega$ (MK3W and Zheng interactions), and $(0+2+4)\hbar\omega$ (Zheng interaction) shell models. The measured energies were obtained from Ref. [5]. All energies are in MeV.

	$J^\pi;T$	Expt.	$0\hbar\omega$		$(0+2)\hbar\omega$		$(0+2+4)\hbar\omega$
			(CK)	(Zheng)	(MK3W)	(Zheng)	(Zheng)
^{6}Li	$1^+;0$	0.000					
	$3^+;0$	2.186	1.410	2.991	2.645	2.876	2.521
	$0^+;1$	3.563	1.935	3.718	1.856	3.578	3.380
^{7}Li	$\frac{3}{2}^-;\frac{1}{2}$	0.000					
	$\frac{1}{2}^-$	0.478	1.282	0.115	0.525	0.472	0.478
	$\frac{7}{2}^-$	4.630	5.713	5.103	5.713	5.871	5.391

state in ^{7}Li in the $0\hbar\omega$ model space are 1.282 and 0.115 MeV for the CK and Zheng shell model calculations.

But inclusion of $2\hbar\omega$ excitations in the model space gives 0.525 MeV and 0.472 MeV for the MK3W and Zheng interactions respectively, suggesting a dramatic convergence in the eigenvalue. The inclusion of $4\hbar\omega$ excitations provides still better agreement, with the result found using the Zheng interaction providing complete agreement with experiment. Similar results are obtained with the other states, although it should be noted that the use of the MK3W interaction in the $(0+2)\hbar\omega$ space for the ^{6}Li spectrum actually worsens the agreement with experiment, with the $0^+;1$ state coming lower in energy compared to the $3^+;0$ state. This is due in part to the use of the Cohen and Kurath $(8-16)$2BME interaction [2] for the $0p$-shell part of the interaction, which is inappropriate for $A < 8$.

As an example of the assessment of the shell model wave functions for ^{6}Li, the longitudinal inelastic scattering form factor to the $3^+;0$ (2.186 MeV) state in ^{6}Li is displayed in Fig. 1. Therein the

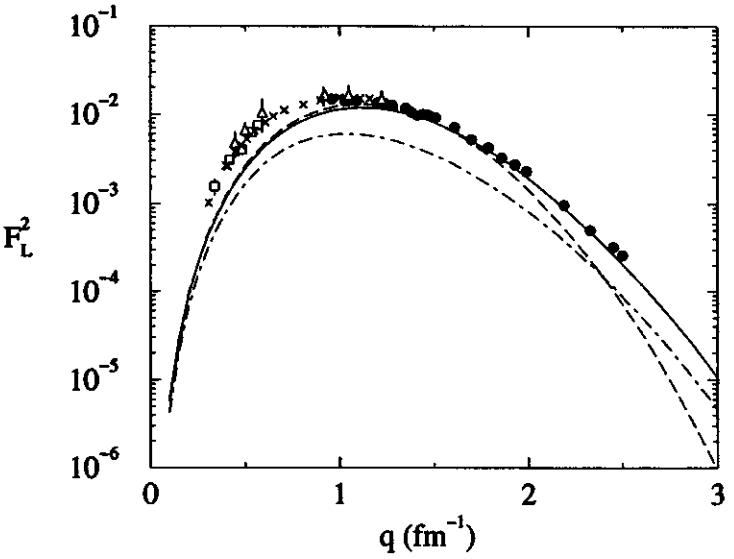

Figure 1: Longitudinal inelastic electron scattering form factor to the $3^+;0$ (2.186 MeV) state in ^{6}Li. The data of Bergstrom *et al.* (circles [6]), of Bergstrom and Tomusiak (crosses [7]), of Yen *et al.* (squares [8]), and of Hutcheon and Caplan (triangles [9]) are compared to the results of the calculations made using the $(0+2+4)\hbar\omega$ (solid line), $(0+2)\hbar\omega$ (dashed line) and $0\hbar\omega$ (dot-dashed line) wave functions.

data of Bergstrom *et al.* (circles [6]), of Bergstrom and Tomusiak (crosses [7]), of Yen *et al.* (squares [8]), and of Hutcheon and Caplan (triangles [9]) are compared to the results of the calculations made using the $(0+2+4)\hbar\omega$, $(0+2)\hbar\omega$, and $0\hbar\omega$ wave functions and which are displayed by the solid, dashed, and dot-dashed lines, respectively. The calculations were predicated on the formalism of deForest and Walecka [10] and single nucleon wave functions of harmonic oscillator (HO) and Woods-Saxon (WS) form were used. The parameters of those bound state potentials were chosen to give a best fit to the longitudinal elastic electron scattering form factor for ^{6}Li. The HO parameters were 1.68 fm, 1.65 fm, and 1.80 fm for the CK, MK3W, and Z4 models respectively. The data above 1 fm^{-1} are well reproduced by both the $(0+2)\hbar\omega$ and $(0+2+4)\hbar\omega$ model calculations, with the $(0+2+4)\hbar\omega$ model fitting the data up to 2.5 fm^{-1}. The failure of the $0\hbar\omega$ model calculation to reproduce the magnitude of the form factor reflects a need for core polarization corrections in that model. Such corrections are included implicitly in the specifications of the larger space models. Nevertheless, all three models underestimate the form factor below 1 fm^{-1}, as

well as the B($E2$) for the decay of this state which empirically is $9.3 \pm 2.1\ e^2\text{fm}^4$ [5]. The values obtained from the shell model calculations are 2.65, 6.03 and 4.07 for the $0\hbar\omega$, $(0+2)\hbar\omega$, and $(0+2+4)\hbar\omega$ models respectively. Low momentum transfer properties of the form factor and the B($E2$) are most influenced by the character of the nuclear wave functions at large radii. Asymptotically, the nuclear wave functions for ^{6}Li should be cluster-like, while the interior reflects largely independent particle motion. Hence, only the interior seems to be well-described by the large space models and none of the models exhibits sufficient (if any) clustering. Even larger space shell models would be required to describe such clustering.

The cross section and analyzing power for the elastic scattering of 200 MeV protons from ^{6}Li is displayed in Fig. 2. Therein the data of Glover *et al.* [11] are compared to the results of the

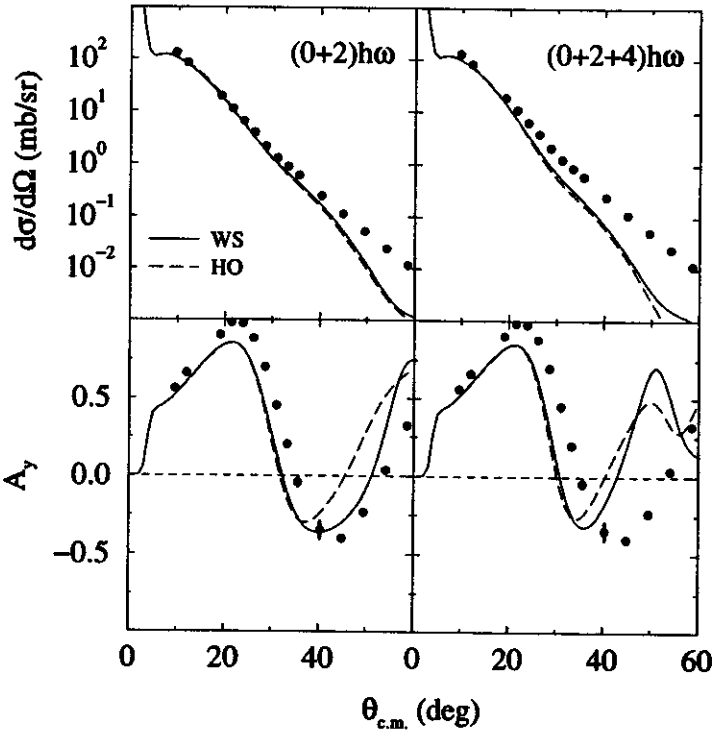

Figure 2: The differential cross section (top) and analyzing power (bottom) for the elastic scattering of 200 MeV protons from ^{6}Li. The data are those of Glover *et al.* [11], while the calculated results displayed by the solid and dashed curves were obtained using Woods–Saxon and harmonic oscillator single nucleon bound state wave functions. The results shown in the left and right panels were obtained using the $(0+2)\hbar\omega$ and $(0+2+4)\hbar\omega$ structure models respectively.

calculations made using the HO and WS single particle wave functions (determined from the elastic longitudinal electron scattering form factor analysis) and which are displayed by the dashed and solid curves respectively. The left-hand panels display the results of the calculations using the $(0+2)\hbar\omega$ wave functions, while those in the right-hand panel display those obtained using the $(0+2+4)\hbar\omega$ wave functions. The density-dependent effective nucleon-nucleus (NA) interaction was derived from the g matrix obtained from the solution of the Brueckner-Bethe-Goldstone equation for infinite nuclear matter [12], and the fully nonlocal optical potential was derived by folding the ground state occupation numbers with the same NA

interaction. The code DWBA91 of Raynal [13] was used to obtain the proton scattering observables in the elastic scattering, and in a distorted wave approximation, also for the inelastic scattering. In the case of the $(0+2)\hbar\omega$ model, agreement is obtained in the cross sections obtained by using both sets of single particle wave functions up to 40°, while the $(0+2+4)\hbar\omega$ result underestimates the data above 20°. This discrepancy is also reflected in the comparisons with the analyzing power data, with the $(0+2)\hbar\omega$ model giving a good reproduction of the data, while the $(0+2+4)\hbar\omega$ model fails above 40°. These problems indicate deficiencies in the structure as the scattering calculations are parameter-free; the nuclear structure input determining the optical potential. A better shell model description of the ground state of ^{6}Li, reflecting the known clustering, is necessary to improve the fit to this scattering data.

The cross section and analyzing power for the inelastic scattering of 200 MeV protons to $3^+;0$ (2.186 MeV) state in ^{6}Li is displayed in Fig. 3, wherein the data of Glover *et al.* (circles) [11] are compared

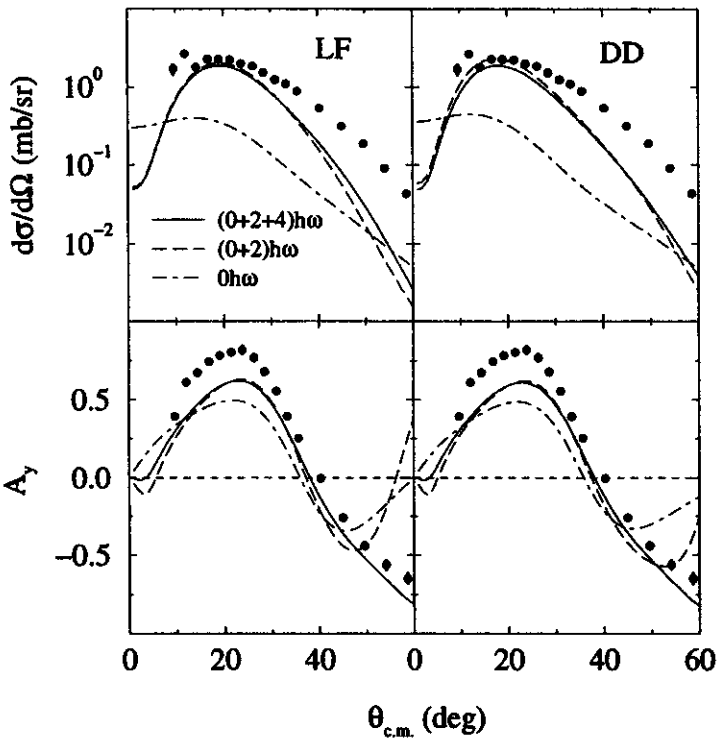

Figure 3: The differential cross sections (top) and analyzing powers (bottom) from the inelastic scattering of 200 MeV protons from ^{6}Li exciting the $3^+;0$ (2.186 MeV) state. The calculations leading to the results displayed in the left and right panels were made using the harmonic oscillator and Woods–Saxon bound state wave functions defined in the text. The data, of Glover *et al.* [11], are compared with results displayed by the short dashed, long dashed and solid curves respectively and which were obtained by using the OBDME from the $0\hbar\omega$, the $2\hbar\omega$, and the $4\hbar\omega$ models of nuclear structure.

to the results of our calculations made using the $(0+2+4)\hbar\omega$, $(0+2)\hbar\omega$, and $0\hbar\omega$ models (solid, dashed, and dot-dashed lines, respectively). In the left hand panels, the results obtained by using harmonic oscillator wave functions are displayed while those in the right hand panels are those found using Woods-Saxon wave functions. As was the case with the electron scattering form factor, the result found by using the

$0\hbar\omega$ structure model wave functions is unable to reproduce the magnitude of the data. Those obtained by using the larger space models are able to reproduce the low-angle part of the cross section but all model results severely underestimate the cross section above 20°. In the case of the analyzing power, all model calculations give reasonable representations of the data, although the $(0+2+4)\hbar\omega$ model does best of all.

Work is in progress to analyze the electron scattering form factors and proton scattering observables to the other states listed in the table.

a. School of Physics, University of Melbourne, Parkville, Vic. 3052, Australia

References

1. D. C. Zheng, B. R. Barrett, J. P. Vary, W. C. Haxton, and C.-L. Song, Phys. Rev. C 52, 2488 (1995).
2. S. Cohen and D. Kurath, Nucl. Phys. 73, 1 (1965).
3. E. K. Warburton and D. J. Millener, Phys. Rev. C 39, 1120 (1989).
4. D. C. Zheng, private communication.
5. F. Ajzenberg-Selove, Nucl. Phys. A490, 1 (1988).
6. J. C. Bergstrom, U. Deutschmann, and R. Neuhausen, Nucl. Phys. A327, 439 (1979).
7. J. C. Bergstrom and E. L. Tomusiak, Nucl. Phys. A262, 196 (1976).
8. R. Yen, L. S. Cardman, D. Kalinsky, J. R. Legg, and C. K. Bockelman, Nucl. Phys. A235, 135 (1974).
9. R. M. Hutcheon and H. S. Caplan, Nucl. Phys. A127, 417 (1969).
10. T. deForest, Jr. and J. D. Walecka, Adv. Phys. 15, 1 (1966).
11. C. W. Glover *et al.*, Phys. Rev. C 41, 2487 (1990).
12. S. Karataglidis, P. J. Dortmans, K. Amos, and R. de Swiniarski, Phys. Rev. C 52, 861 (1995).
13. J. Raynal, computer code DWBA91 (NEA1209/02).

STRENGTH FUNCTIONS OF SHELL MODEL BASIS STATES

Njema Frazier, B. Alex Brown, and Vladimir Zelevinsky

One of the most important characteristics of many-body dynamics is given by the strength function of simple modes. Due to the residual interaction, highly excited simple configurations are mixed with the background of fine structure states. Treating this background as a continuum, one would expect the exponential decay of the original excitation, and, therefore, a Breit-Wigner shape for its strength distribution. A microscopic mechanism for the coupling between the simple mode and its chaotic environment leading to the Breit-Wigner strength function is explained in detail in [1]. This "standard" model is valid [2] in the case of weak coupling when the spreading width is small compared to the interval where the level density and/or mixing matrix elements change significantly.

Studying the fragmentation of simple configurations as a function of excitation energy and interaction strength in the framework of the nuclear shell model, we are able to check in detail various statistical hypotheses. Our statistics allow us to establish for the first time the generic shape of the strength function in the region of strong mixing.

The fragmentation of simple configurations was studied as a function of excitation energy and interaction strength for 839 states with quantum numbers $J^\pi T = 0^+0$ in the system of 12 valence particles within the *sd*-shell. The system can be considered as a model for the ^{28}Si nucleus in the approximation when the interaction across the major shells is neglected. The calculations are carried out with the OXBASH code [3] using the Wildenthal hamiltonian.

In the traditional basis of the independent particle shell model, the hamiltonian

$$H = H_o + H' \tag{1}$$

contains the unperturbed configuration energies, given by H_o, and the residual interaction H'. To remove the degeneracy of the shell model configurations, it is convenient to include the diagonal part of the residual interaction into the unperturbed hamiltonian. Its eigenfunctions satisfy

$$H_o|k\rangle = \bar{E}_k|k\rangle \tag{2}$$

where $\bar{E}_k = H_{kk}$. By the diagonalization of the full hamiltonian matrix including the off-diagonal matrix elements H'_{kl}, we obtain the eigenstates $|\alpha\rangle$ and their energies E_α,

$$H|\alpha\rangle = E_\alpha|\alpha\rangle. \tag{3}$$

The eigenstates are the complicated superpositions

$$|\alpha\rangle = \sum_k C_k^\alpha |k\rangle \tag{4}$$

of the basis shell model states $|k\rangle$. The fragmentation of basis states, $|k\rangle = \sum_\alpha C_k^\alpha|\alpha\rangle$, is described by the same (real due to the time reversal invariance) transformation coefficients C_k^α.

The average characteristics of the fragmentation can be expressed directly in terms of the matrix elements of the hamiltonian (1). For a given basis state $|k\rangle$, the centroid of the strength distribution

coincides with the unperturbed energy (2),

$$\sum_{\alpha}(C_k^{\alpha})^2 E_{\alpha} = \bar{E}_k. \tag{5}$$

The second moment of the strength distribution is determined by the sum of all off-diagonal matrix elements (starting at a given basis state) squared,

$$\sigma_k^2 \equiv \sum_{\alpha}(C_k^{\alpha})^2(E_{\alpha} - \bar{E}_k)^2 = \sum_{l\neq k}(H'_{kl})^2. \tag{6}$$

All the moments of the strength distribution can be found from the strength function

$$F_k(E) = \sum_{\alpha}(C_k^{\alpha})^2 \delta(E - E_{\alpha}). \tag{7}$$

As compared to the full density of states

$$\rho(E) = \sum_{\alpha}\delta(E - E_{\alpha}), \tag{8}$$

the strength function (7) is frequently called the "local density of states." It determines the contribution of the basis state $|k\rangle$ to $\rho(E)$ at $E = E_{\alpha}$,

$$F_k(E) = \rho(E)\langle(C_k^{\alpha})^2\rangle_{E_{\alpha}=E}. \tag{9}$$

The level density (8) has a Gaussian shape with the variance $\sigma_E = 13$ MeV at realistic interaction strength. It is known [4,5] that the Gaussian shape occurs mainly due to combinatorial reasons for the two-body interaction in the many-body system.

Fig. 1 shows the "empirical" strength functions $F_k(E)$, eq.(9), for nine basis states $|k\rangle$ with the centroids $\bar{E}_k$ located in the middle of the spectrum. The histograms are plotted as a function of the energy distance from the corresponding centroid. We superimpose the strength functions of 400 basis states in the middle of the spectrum in order to reduce the statistical fluctuations and produce a smooth "generic" strength function. Its shape, Fig. 2, is different from the Breit-Wigner one and, except for the wings, can be described by the Gaussian with the dispersion $\sigma_F = 8.9 \pm 0.7$ MeV. The typical spreading width (FWHM) of the central 0^+0 states equals $\Gamma = (8\ln 2)^{1/2}\sigma_F = 21$ MeV. We see that the realistic interaction strength leads to the so-called strong coupling case [2] when the large spreading width exceeds the energy interval where the level density and mixing matrix elements can be considered constant.

According to eq.(9), the strength function histograms actually involve two factors, the average value $\langle(C_k^{\alpha})^2\rangle$ of the eigenfunction components corresponding to the basis state $|k\rangle$, and the level density $\rho(E)$. The level density itself is described [6] by a Gaussian curve. The level density effects dominate the central part of the strength function. It is clear from Fig. 3, especially from the logarithmic plot of Fig. 3*b*, that an exponential fit represents the tails of the strength distribution. The final form of this fit is

$$F_k(E - \bar{E}_k) \approx F_0 \exp\Big(-\frac{E - \bar{E}_k}{E_l}\Big) \tag{10}$$

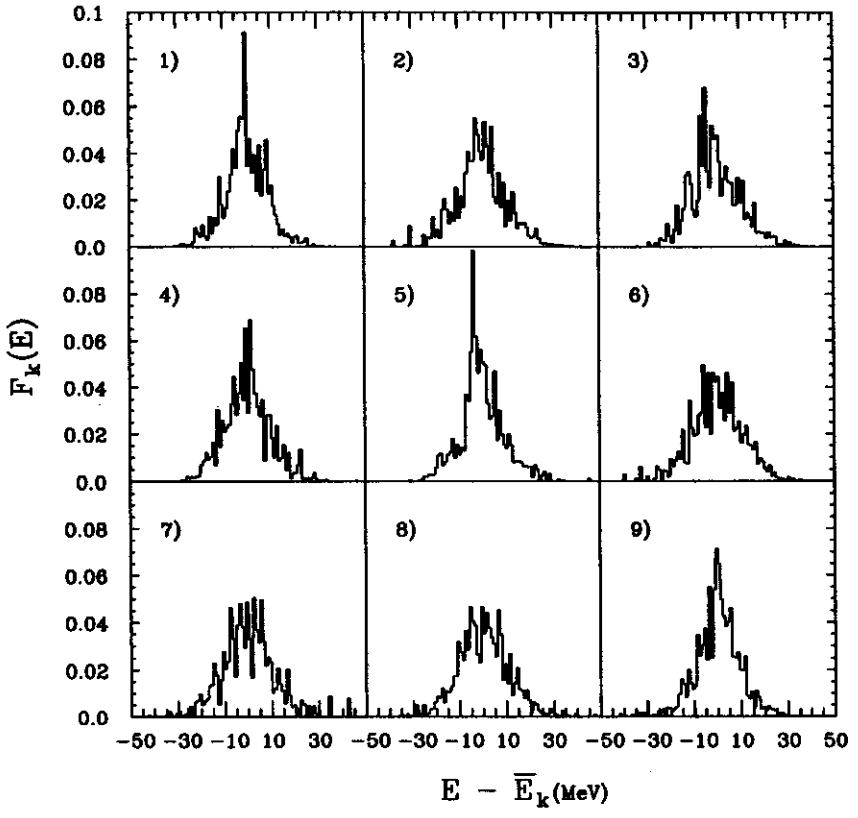

Figure 1: The strength functions for 9 individual 0^+0 basis states $|k\rangle$ in the middle of the spectrum (histograms) *vs* the energy distance, $E - \bar{E}_k$, from the centroid of the unperturbed state $|k\rangle$, panels *1 - 9*. The bin size is 1 MeV.

where the energy localization length is $E_l = 5$ MeV. Of course, the expression (10) is valid only for the tails of the distribution, $(E - \bar{E}_k) > \Gamma$. The exponential behavior holds for at least three orders of magnitude.

To conclude, the strength function for stationary nuclear states was, for the first time, extracted from the exact solution of the many-body problem in the truncated Hilbert space of shell-model configurations. The realistic interaction strength corresponds to the strong coupling case. The generic shape of the compound states at high excitation energy is close to a Gaussian but with exponential wings.

References

1. A.Bohr and B.Mottelson, *Nuclear Structure*, vol. 1 (Benjamin, New York, 1969).
2. B.Lauritzen, P.F.Bortignon, R.A.Broglia and V.Zelevinsky. Phys. Rev. Lett. 74, 5190 (1995).
3. B.A.Brown *et al.*, *OXBASH code*, MSUNSCL Report 524 (1988).
4. T.A.Brody, J.Flores, J.B.French, P.A.Mello, A.Pandey and S.S.M.Wong, Rev. Mod. Phys. 53, 385 (1981).
5. K.K.Mon and J.B.French, Ann. Phys. 95, 90 (1975).
6. V.Zelevinsky, B.A.Brown and M.Horoi, Phys. Lett. B350, 141 (1995); V. Zelevinsky, B. A. Brown, N. Frazier and M Horoi, Phys. Reports, in press.

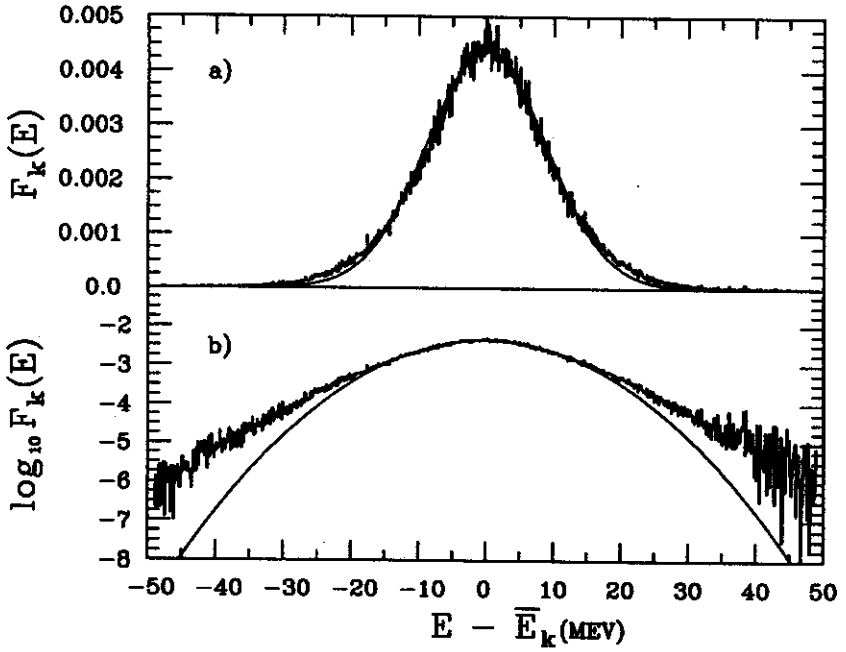

Figure 2: The Gaussian fit (solid lines) to the the strength function averaged over 400 states, panel a, and the same fit on the logarithmic scale, panel *b*. The bin size is 100 keV.

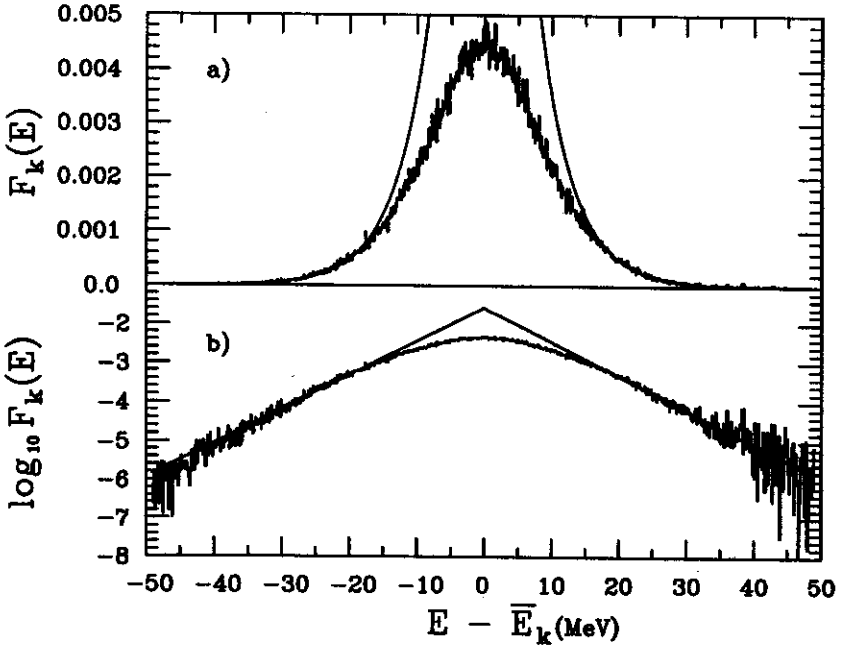

Figure 3: The exponential fit of eq.(10), solid lines, to the wings of the strength function of Fig. 2, a (histograms), panel a, and the same fit on the logarithmic scale, panel *b*. The bin size is 100 keV.

SPREADING WIDTHS OF SIMPLE SHELL MODEL CONFIGURATIONS

Njema Frazier, B. Alex Brown, and Vladimir Zelevinsky

The detailed analysis of the spreading widths of the basis shell model configurations as a function of the interaction strength allowed us for the first time to trace the transition from the weak to strong coupling case, see the preceding report [1]. The existence of these two limits was recognized long ago by Wigner [2] and discussed in the banded random matrix models [3]. The description of both limits under the assumption of uniformity of basis states was suggested in [4]. The deviations from the standard model [5], which is based on the weak coupling, are responsible [6,7] for the narrow width of the double giant resonances [8].

The standard model leads to the Breit-Wigner shape of the strength function. The spreading width in this model is given by the golden rule,

$$\Gamma_s = 2\pi \frac{\langle V^2 \rangle}{D}. \tag{1}$$

Here $\langle V^2 \rangle$ is the average coupling intensity of the given basis state to the fine structure background which is characterized by the average level spacing D. The standard model is correct as long as the resulting spreading width is relatively small. It should be compared with the energy range ΔE within which the level density and the coupling matrix elements can be considered as approximately constant. One can estimate what happens as the coupling strength and the spreading width increase by assuming that the coupling $V_{k\nu}^2$ of a given basis state $|k\rangle$ with the background states $|\nu\rangle$ vanishes at some finite distance $\Delta E = e_\nu - \bar{E}_k$ from the centroid $\bar{E}_k$. This leads to a simple estimate for the spreading width in the limit of complete mixing

$$\Gamma_k \approx 2\sigma_k \tag{2}$$

where σ_k is the energy dispersion of the basis state $|k\rangle$ calculated as a sum of squared off-diagonal matrix elements starting from this state, see eq.(6) in [1]. This estimate gives $\Gamma \approx 20$ MeV for the $J^\pi T = 0^+0$ states in the *sd* shell model which we used in our analysis. In contrast to the standard model, eq.(2) predicts the linear dependence of the spreading width on the interaction strength; at the realistic strength $\bar{\sigma}_k \approx 10$ MeV, and $\Gamma \approx 21$ MeV, in agreement with (2).

We study the evolution of the strength function and the spreading width as a function of the residual interaction λ. The scale λ is defined as a common factor in front of the residual off-diagonal interaction H' - $H = H_o + \lambda H'$; $\lambda = 1$ corresponds to the realistic strength. The transition from the weak to strong coupling can be described by the interpolation formula

$$\Gamma = \frac{\gamma \lambda^2}{1 + y\lambda} \tag{3}$$

where γ and y can be estimated in terms of the shell model parameters.

As was shown in [9], the shell model level statistics reveal standard signatures of quantum chaos already at $\lambda \approx 0.2$. At weak interaction strength, the shape of the strength function is close to the Breit-Wigner one. The evolution pattern is seen in Fig. 1, panels 1a - 1*d*. The Breit-Wigner description of the main part of the strength function can be considered as satisfactory up to $\lambda \approx 0.4$. In this region the

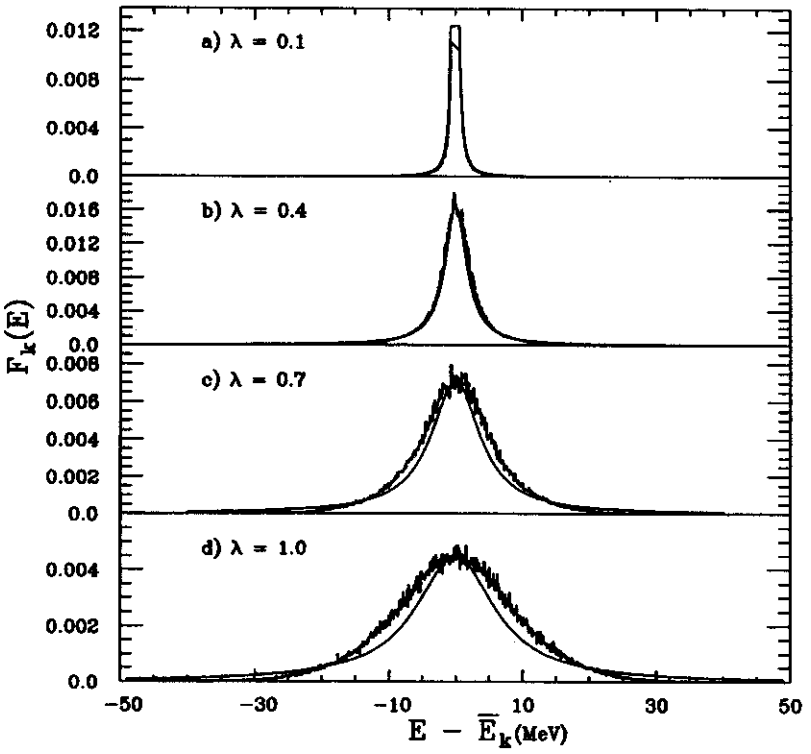

Figure 1: Breit-Wigner fit (solid lines) to the strength function averaged over 400 0^+0 mid-energy states for λ = 0.1, 0.4, 0.7, and 1.0, panels a, *b*, *c* and *d*, respectively. The bin size is 100 keV.

narrow strength function is not strongly influenced by the change of the level density. As seen from Fig. 2, the quality of the Gaussian fit clearly improves as one goes to the strong coupling limit; the last panel, 2*d*, corresponds to $\lambda = 1.2$. Using "empirical" generic strength functions found in [1], we can trace the evolution of the spreading width (FWHM). Fig. 3 shows the results for the values of λ between 0 and 1.2. The dependence of the spreading width on the interaction changes from quadratic in the weak coupling limit to linear at strong coupling. The results are nicely described by the simple interpolation (3) with parameters $\gamma \approx 44.9$ MeV and $y \approx 1.32$. Our estimates, using the value of the average level spacing at weak interaction $D_0 \approx 21$ keV, predict for these parameters $\gamma = 44.6$ MeV and $y = 1.23$.

We conclude that the transition to the weak coupling case at the artificially suppressed strength of the residual interaction shows how the shape of the strength function regularly changes from the Gaussian to the "normal" Breit-Wigner. This is accompanied by the reduction of the spreading width and the smooth transition from the linear interaction dependence characteristic for the strong coupling limit to the ordinary quadratic dependence predicted by the golden rule. This transition is seen for the first time in realistic calculations.

References

1. N.Frazier, B.A.Brown and V.Zelevinsky, this Annual Report.
2. E.P.Wigner, Ann. Math. 62, 548 (1955).
3. M.Feingold, A.Gioletta, F.M.Izrailev and L.Molinari, *to be published.*

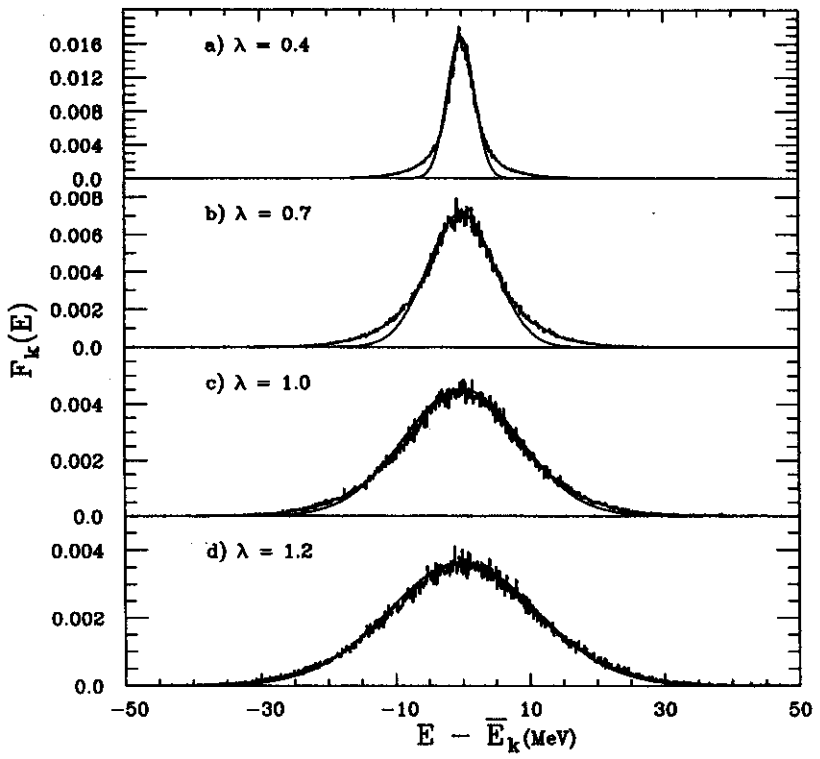

Figure 2: Gaussian fit to the strength function averaged over 400 0^+0 mid-energy states for $\lambda = 0.4$, 0.7, 1.0, and 1.2, panels a, *b*, *c* and *d*, respectively.

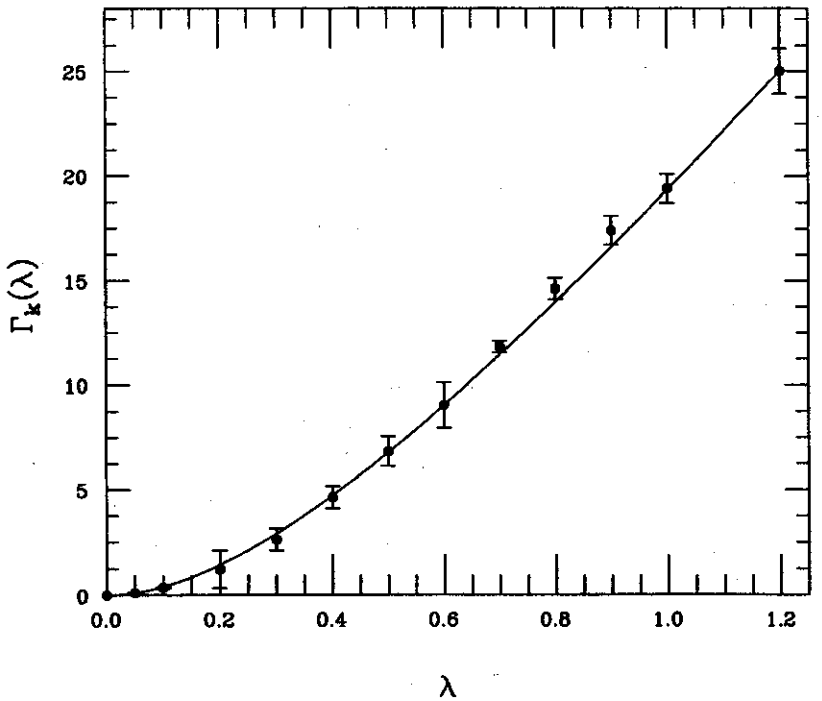

Figure 3: Spreading width Γ_k of the basis states as a function of the interaction strength λ for 400 middle 0^+0 states. The solid line corresponds to eq.(3) with $\gamma = 44.9$ MeV and $y = 1.32$. The error bars are defined by the deviations of the fit from the calculated data.

4. B.Lauritzen, P.F.Bortignon, R.A.Broglia and V.Zelevinsky. Phys. Rev. Lett. 74, 5190 (1995).
5. A.Bohr and B.Mottelson, *Nuclear Structure*. Vol. 1 (Benjamin, New York, 1969).
6. C.A.Bertulani and V.G.Zelevinsky, Phys. Rev. Lett. 71, 967 (1993); Nucl. Phys. A568, 931 (1994).
7. C.H.Lewenkopf and V.G.Zelevinsky, Nucl. Phys. A569, 183 (1994).
8. S.Mordechai *et al.*, Phys. Rev. C41, 202 (1990); J.Ritman *et al.*, Phys. Rev. Lett. 70, 533 (1993); R.Schmidt *et al.*, Phys. Rev. Lett. 70, 1767 (1993); T.Aumann *et al.*, Phys. Rev. C47, 1728 (1993).
9. V.Zelevinsky, M.Horoi andf B.A.Brown. Phys. Lett. B350, 141 (1995).

PLAUSIBLE STRUCTURES OF MULTIPLE SEMI-IDENTICAL SUPERDEFORMED BANDS IN ^{132}Pr

W.A. Olivier, C.V. Hampton, and Wm.C. McHarris

In a previous report we observed the existence of multiple superdeformed bands in the ^{132}Pr nucleus with very similar rotational energy spacings.[1] These bands were termed "semi-identical" to denote the high degree of similarity among them, though they did not meet the generally accepted criteria for "Identical Bands." In this report, we propose specific structures for semi-identical bands in ^{132}Pr nuclide based on either cranked shell model (CSM) calculations using a Woods-Saxon potential[2] or more intuitively, on systematics of occupied orbitals observed in neighboring nuclides.

A series of total Routhian surface (TRS)[3] calculations of plausible structures for ground state configurations of ^{132}Pr was performed. The calculations showed, for nearly all possible configurations, the ^{132}Pr nucleus exists as a well-behaved prolate rotor (though somewhat soft to triaxial deformations) with the β_2 deformation parameter ranging from 0.2 to 0.35 and β_4 and γ parameters centered near zero values for these structures. Figure 1 illustrates two sample TR surfaces at a nominal rotational frequency of 0.3 $\hbar^2$/MeV.

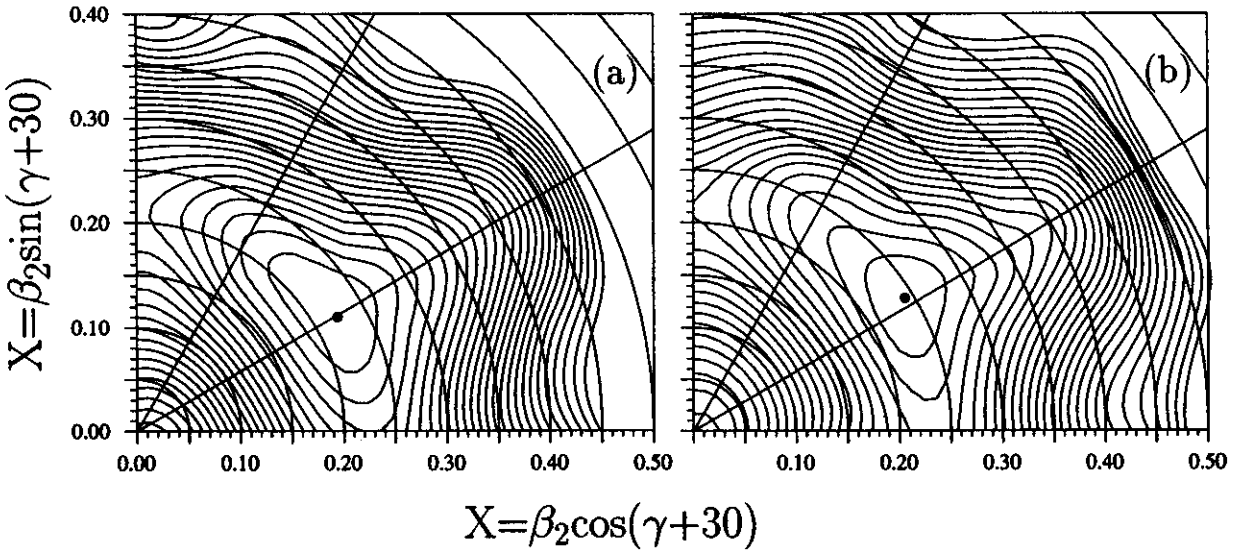

Figure 1: Two total Routhian surfaces: (a) Neutron occupies the lowest availible negative parity – positive signature orbital (-,+) while the proton occupies the lowest (-,-) orbital, (b) The neutron (+,-), proton (-,+) configuration.

The results of TRS calculations, in addition to providing a survey of general trends of shape and shape stability of the nuclide, were used to extract specific deformation information to calculate Routhians of proton and neutron structures for "realistic" conditions. Figure 2 shows single particle Routhians as a function of rotational frequency for protons and neutrons at β_2=0.30, β_4=-0.004, and γ=0.00.

Given these deformation parameters, we observe the ground state configuration consists of a $g_{7/2}$ neutron coupled to an $h_{11/2}$ proton. The observation of these specific configurations are not extremely important to the current evaluation.

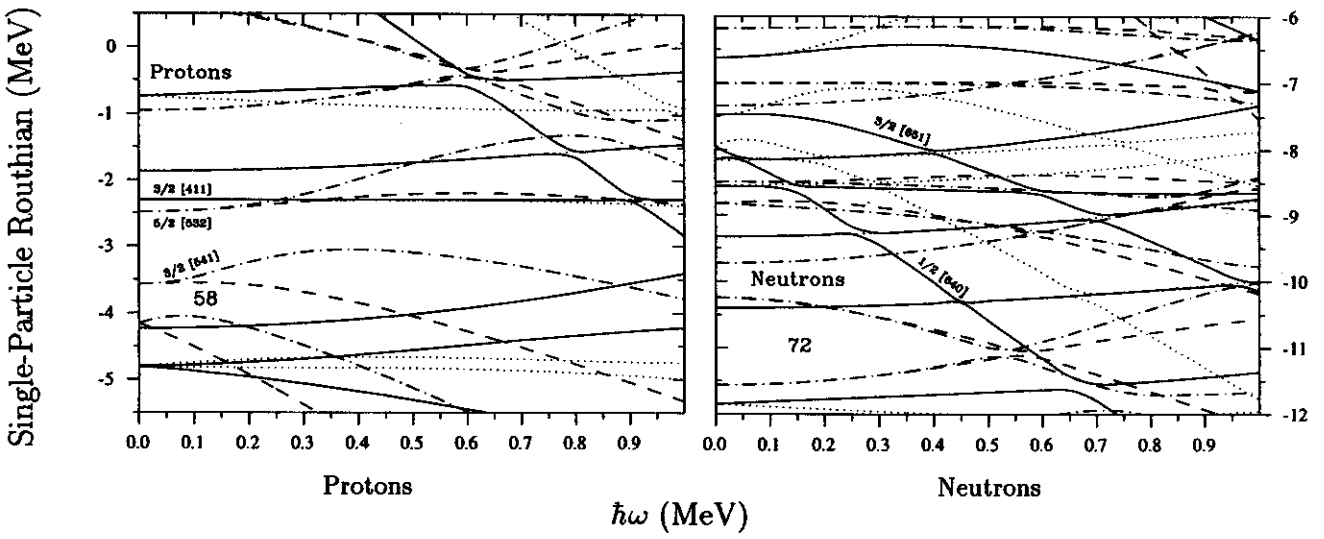

Figure 2: Single particle Routhians calculated at β_2=0.30 β_4=-0.004 and γ=0.0 Routhians for particles of particular interest are labeled. All Routhians follow the convention of (parity,signature) (π,α) are denoted: solid=(+,+), dot=(+,-), dot-dash=(-,+), and dash=(-,-). (a) Protons with blocking of the lowest (-,+) level and (b) Neutrons with blocking of the lowest (+,-) level.

The more important aspect of the calculations is the usefulness in identification of highly deformation-driving orbitals which lie within a few MeV above the Fermi surface. These are the prime candidates for components of bandhead structures of SD bands.

No such orbitals exist for proton excitations to encourage a more deformed structure until rotational frequencies on the order of 0.8 MeV are achieved. At this point the highly mixed "$g_{9/2}$ 1/2[651]" crosses the $d_{5/2}$ 3/2[411] and becomes low enough in energy to be populated. It is doubtful that this band crossing comes into play in the rotational structure of SD bands. Most of the available proton orbitals are fairly constant in excitation energy, both in terms of rotational frequency and quadrupole deformations. They would serve only to hold "spectator" nucleons and provide several similar states which can be occupied to construct semi-identical bandhead configurations. These include the positive parity $g_{7/2}$ 5/2[413] and $d_{5/2}$ 3/2[411] as well as the negative parity $h_{11/2}$ 5/2[532].

The neutrons in this region however, do have several highly mixed, but very good candidates for high deformation effects. An intruder $i_{13/2}$ 3/2[651] and the $i_{11/2}$ 1/2[640] orbital diving in from the next shell both show significant decreases in single-particle energies with increased rotational frequency.

There are not many good candidates for well characterized "neighbors" with SD type structures around the ^{132}Pr nucleus. The most promising structures appear to be similar to the decoupled and doubly-decoupled bands which tend to be built on opposite parity orbitals from the next oscillator shell. An example of this behavior is found in the ^{134}Pm nucleus.[4] It is most likely the SD structures in ^{132}Pr have similar types of highly aligned $h_{9/2}$ or at least aligned negative parity 5^{th} shell neutron contributions coupled to static proton structures from the 4^{th} shell.

References

1. C.V. Hampton, R. Aryaeinejad, W.A. Olivier, R. Ronningen, Wm.C. McHarris, and ORNL Nuclear Structure Research Group, NSCL/MSU Annual Report, 99 (1994)
2. W. Nazarewicz, J. Dudek, R. Bengtsson, and I. Ragnarsson, Nucl. Phys. A435, 397 (1985)
3. R. Wyss, J. Nyberg, A. Johnson, R. Bengtsson, and W. Nazarewicz, Phys. Lett. B. 215, 211 (1988)
4. R. Wadsworth, S.M. Mullins, P.J. Bishop, A. Kirwan, M.J. Godfrey, P.J. Nolan, and P.H. Regan, Nucl. Phys. A526, 188 (1991)